



## Polar amplification of orbital-scale climate variability in the early Eocene greenhouse world

Chris D. Fokkema<sup>1</sup>, Tobias Agterhuis<sup>1</sup>, Danielle Gerritsma<sup>1</sup>, Myrthe de Goeij<sup>1</sup>, Xiaoqing Liu<sup>2</sup>, Pauline de Regt<sup>1</sup>, Addison Rice<sup>1</sup>, Laurens Vennema<sup>1</sup>, Claudia Agnini<sup>3</sup>, Peter K. Bijl<sup>1</sup>, Joost Frieling<sup>4</sup>, Matthew Huber<sup>2</sup>, Francien Peterse<sup>1</sup> and Appy Sluijs<sup>1</sup>

<sup>1</sup>Department of Earth Sciences, Faculty of Geosciences, Utrecht University, 3584CB Utrecht, The Netherlands.

<sup>2</sup>Earth, Atmospheric, and Planetary Sciences Department, Purdue University, West Lafayette, IN 47907-2051.

10 <sup>3</sup>Dipartimento di Geoscienze, Università degli Studi di Padova, I-35131 Padova, Italy.

<sup>4</sup>Department of Earth Sciences, University of Oxford, Oxford, OX1 3AN, United Kingdom.

Correspondence to: Chris D. Fokkema (c.d.fokkema@uu.nl)

**Abstract.** Climate variability is typically amplified towards polar regions. The underlying causes, notably albedo and humidity changes, are challenging to accurately quantify with observations or models, hampering projections of future polar amplification. Polar amplification reconstructions from the ice-free early Eocene (~56–48 million years ago) can exclude ice albedo effects, but the required tropical temperature records for resolving timescales shorter than multi-million years are lacking. Here, we reconstruct early Eocene tropical sea surface temperature variability by presenting an up to ~4 kyr-resolution biomarker-based temperature record from Ocean Drilling Program Site 959, located in the tropical Atlantic Ocean. This record shows warming across multiple orbitally paced carbon cycle perturbations, coeval with high-latitude-derived deep-ocean bottom waters, showing that these events represent transient global warming events (hyperthermals). This implies that orbital forcing caused global temperature variability through carbon cycle feedbacks. Importantly, deep-ocean temperature variability was amplified by a factor 1.7–2.3 compared to the tropical surface ocean, corroborating available long-term estimates. This implies that fast atmospheric feedback processes controlled meridional temperature gradients on multi-million year, as well as orbital timescales during the early Eocene.

25 Our combined records have several other implications. First, our amplification factor is somewhat larger than the same metric in fully-coupled simulations of the early Eocene (1.1–1.3), suggesting that models slightly underestimate the non-ice related — notably hydrological — feedbacks that cause polar amplification of climate change. Second, even outside the hyperthermals, we find synchronous eccentricity-forced temperature variability in the tropics and deep ocean that represent global mean sea surface temperature variability of up to 0.7 °C, and requires significant variability in atmospheric  $p\text{CO}_2$ . We

30 hypothesize that the responsible carbon cycle feedbacks that are independent of ice, snow and frost-related processes might play an important role in Phanerozoic orbital-scale climate variability throughout geological time, including Pleistocene glacial-interglacial climate variability.



## 1. Introduction

The inverse relationship between Earth's meridional temperature gradient (MTG) and mean surface temperature is a feature of global climate change, often termed polar amplification (PA) (e.g., Masson-Delmotte et al., 2013). Polar amplification — here defined as the ratio of high-latitude ( $>60^\circ$ ) to low-latitude ( $<30^\circ$ ) warming — is attributed to various climate feedback mechanisms. These feedback mechanisms can be grouped into two categories: 1) surface-albedo changes, mostly from ice, snow and vegetation, and, 2) ocean-atmosphere processes, including the lapse rate feedback, longwave cloud and moisture feedbacks and changes in poleward heat transport (Deconto et al., 1999; Caballero, 2005; Held and Soden, 2006; Stuecker et al., 2018). Together with the more common focal points of climate sensitivity and global emission trajectories, PA will determine the magnitude of future high-latitude warming and therefore influences the rate of sea level rise through polar ice sheet melt and the dynamics of several carbon cycle feedbacks, such as permafrost thawing (Masson-Delmotte et al., 2013). At present, amplified warming is already observed in the Arctic (England et al., 2021), but the observational timespan of a few decades is still insufficient to decipher the different contributing feedbacks to PA or project future PA, as many “slow” feedbacks take place on  $10^2$ – $10^4$  year timescales (e.g., continental icesheets). Furthermore, climate models produce very different or even contrasting results (e.g., a dominant (Taylor et al., 2013a) versus minor (Stuecker et al., 2018) contribution of the albedo feedback to PA), which cannot be validated due to a lack of observational ground truthing. Additionally, in the presence of icesheets, interaction between the ice-albedo effect and local influences of the icesheet interfere, masking ice-unrelated processes of PA.

Reconstructions of PA during ice-free climates in the geological past may, in part, overcome the lack of proper analogues in observations. Earth's most recent ice-free climate state occurred in the early Eocene (56–48 million years ago (Ma)), a time characterized by globally elevated temperatures, exceptionally low MTGs and high atmospheric  $\text{CO}_2$  concentrations (Cramwinckel et al., 2018; Anagnostou et al., 2020; Gaskell et al., 2022). Ice sheets were insignificant or absent given overall low deep-ocean benthic foraminifer oxygen isotope ( $\delta^{18}\text{O}$ ) values (Zachos et al., 2001). Biotic and geochemical evidence also point to frost-free winters and even subtropical conditions in the Arctic realm (Willard et al., 2019; Sluijs et al., 2020), as well as the Southern Ocean coastal and near-shore regions in Antarctica (Pross et al., 2012; Bijl et al., 2013, 2021). Long-term warmth peaked during the Early Eocene Climatic Optimum (EECO;  $\sim 53$ –49 Ma), when the global mean surface temperature reached values of 10–16 °C higher than pre-industrial (Inglis et al., 2020). Since ice-related albedo feedbacks did not occur on fast timescales within the early Eocene, reconstructing PA of climate change during this period may help disentangle the contribution of surface albedo and non-albedo feedbacks.

Recent work has documented a gradual strengthening of the MTG between the early Eocene and the Oligocene, coeval with the multi-million-year  $p\text{CO}_2$  decline and global cooling trend (Evans et al., 2018; Cramwinckel et al., 2018; Anagnostou et al., 2020; Gaskell et al., 2022). Much of this work estimated the MTG by comparing tropical sea surface temperature (SST) records to benthic foraminiferal  $\delta^{18}\text{O}$ -based bottom water temperatures (BWTs). The underlying assumption to this approach is that Eocene BWTs reflect Southern Ocean SSTs (specifically that of subpolar gyres), consistent with climate proxy data



(Cramwinckel et al., 2018; Gaskell et al., 2022) and model simulations (Hollis et al., 2012; Zhang et al., 2020). Indeed, multi-million-year climate trends and its PA have now been demonstrated to dominantly represent long-term variability in atmospheric greenhouse gas concentrations and associated feedbacks (Cramwinckel et al., 2018). This low-resolution work has shown that in the absence of ice-albedo feedbacks,  $10^6$ -year-timescale climate change was amplified in the southern high latitudes with a constant and linear PA factor of 1.2–2.2 (Cramwinckel et al., 2018; Gaskell et al., 2022).

Given that different timescales have different associated climate feedback mechanisms (PALAEOSENS Project Members, 2012), the current  $10^6$ -year reconstructions of past PA (Cramwinckel et al., 2018; Gaskell et al., 2022; Liu et al., 2022) are incomparable to present-day climate change on  $10^2$ – $10^3$  year timescales. While we acknowledge that the paleoclimate record cannot approach the current rates of change, records of past orbitally forced climate change may provide the closest possible approximation of PA on shorter ( $10^3$ – $10^4$ -year) timescales.

Numerous carbon cycle perturbations, most, if not all, paced by orbital eccentricity, accentuated early Eocene global warmth (Cramer et al., 2003; Lourens et al., 2005; Westerhold et al., 2018; Lauretano et al., 2018) and present suitable targets for  $10^3$ – $10^4$ -year PA assessment. These events are recognized in the sedimentary record by distinct negative stable carbon isotope ( $\delta^{13}\text{C}$ ) excursions (CIEs) (Cramer et al., 2003) and carbonate dissolution in deep-ocean sedimentary environments (Leon-Rodriguez and Dickens, 2010), linked to the release of voluminous  $^{13}\text{C}$ -depleted carbon into the ocean-atmosphere system (Dickens et al., 1997). Several of these events have been shown to represent transient global warming phases, notably the Paleocene-Eocene Thermal Maximum (PETM; ~56 Ma) (Kennett and Stott, 1991; Frieling et al., 2017; Tierney et al., 2022) and Eocene Thermal Maximum 2 (ETM-2; ~54 Ma) (Lourens et al., 2005; Harper et al., 2018). For the PETM, which received most attention among these so-called ‘hyperthermals’ (Thomas and Zachos, 2000), reconstructions show rapid global warming of ~5 °C (Frieling et al., 2017; Tierney et al., 2022), ocean acidification and acceleration of the hydrological cycle and biotic change (Zachos et al., 2005; McInerney and Wing, 2011; Carmichael et al., 2017). Similar changes, yet of smaller magnitude, characterize ETM-2 (Stap et al., 2009, 2010; Sluijs et al., 2009; Gibbs et al., 2012; Harper et al., 2018). Quantification of (global) SST change is, however, challenging for ETM-2 and the subsequent post-PETM hyperthermals due to a lack of decent-resolution (tropical) SST records. Consequently, only for the PETM, reasonable estimates of millennial-scale PA are available, arriving at 1.7–2.7 (Frieling et al., 2017) and ~1.6 (Tierney et al., 2022). While high-latitude surface warming can be quantified for the subsequent hyperthermals by state-of-the-art benthic  $\delta^{18}\text{O}$  compilations on timescales of  $10^3$ -years (Cramwinckel et al., 2018; Gaskell et al., 2022), estimation of PA on this timescale remains impossible as long as the response of the tropical endmember is unknown.

Here, our aim is to solve the lack of high-resolution tropical climate constraints and consequently allow reconstruction of early Eocene  $10^4$ -year timescale PA. Accordingly, we produced up to ~4-kyr resolution  $\text{TEX}_{86}$ -based SST records over a ~2 Myr early Eocene interval from Ocean Drilling Program (ODP) Leg 159 Site 959 (equatorial Atlantic, paleolatitude = ~9 °S (paleolatitude.org version 2.1; van Hinsbergen et al., 2015)), covering multiple early Eocene carbon cycle events. While ideally multiple sites are averaged to track climate variations over a complete latitudinal band, previous work on Site 959 showed that long-term ( $10^6$ -year) Eocene (Cramwinckel et al., 2018) and short-term ( $10^3$ -year) PETM (Frieling et al., 2019) biomarker-



100 based SST records provide a good representation of climate variability in the complete tropical band. Moreover, IPCC-class  
fully coupled climate models, forced by a range of  $p\text{CO}_2$  values from 1x to 8x pre-industrial values under early Eocene  
boundary conditions (no ice and continental configuration) within the Deep-Time Model Intercomparison Project (DeepMIP)  
(Lunt et al., 2021) indicate that the SSTs at the location of Site 959 vary equally to SSTs in the complete tropical band under  
105 Eocene CIEs indeed represent global warming phases and assess how equatorial SSTs varied during a series of suspected early  
Eocene hyperthermals. Subsequently, we estimate ice-free PA on orbital timescales ( $10^4$ -years) by comparing equatorial SST  
variability to a benthic  $\delta^{18}\text{O}$ -based deep-ocean temperature compilation (Westerhold et al., 2020).

## 2. Materials and Methods

### 2.1 Sample location, sampling and approach

110 Lower Eocene sediments were retrieved in 1995 during ODP Leg 159 at Site 959 Hole D. Site 959 is located in the eastern  
equatorial Atlantic, ~150 km offshore of Ghana ( $3^\circ37.656'\text{N}$ ;  $2^\circ44.149'\text{W}$ ), on a northward dipping slope of the Cote d'Ivoire-  
Ghana Transform Margin at 2091 m water depth (Masclé et al., 1996). The lower Eocene pelagic sediments comprise  
dominantly diagenetically altered biogenic silica, carbonate and clay, with some organic matter, ranging from soft bioturbated  
greyish micritic clay-bearing sediments to hard white, carbonate-lean porcellanitic sediments with abundant in situ pyritic  
115 concretions (Masclé et al., 1996; Wagner, 2002).

Following the existing age model that is based on the identification of the PETM (Frieling et al., 2019) and the Middle Eocene  
Climatic Optimum (van der Ploeg et al., 2018) as well as biostratigraphy (Cramwinckel et al., 2018), Cores 41R to 38R (800.5–  
764.2 mbsf) were completely sampled at 2-cm resolution (1143 samples). Samples were freeze dried and cleaned from visible  
120 hyperthermals and orbital cyclicity using bulk rock magnetic susceptibility, various bulk rock geochemical parameters and  
calcareous nannofossil biostratigraphy. Subsequently, we perform high-resolution  $\text{TEX}_{86}$  paleothermometry to assess tropical  
SST variability and broadly assess local ecosystem variability using palynology to exclude an influence of local oceanographic  
variability on our SST estimates. All analyses were carried out at Utrecht University unless stated otherwise.

Finally, PA of climate change was assessed by comparison between Site 959  $\text{TEX}_{86}$  and a  $\delta^{18}\text{O}$ -based deep-ocean temperature  
125 compilation ('CENOGRID') (Westerhold et al., 2020). Calculation of  $10^4$ -year timescale PA by directly comparing two  
records relies on accurate stratigraphic correlation and inaccuracies can already arise from smaller-scale stratigraphic  
correlation related errors, even if an age model is constrained on the scale of (100-kyr) orbital eccentricity. Therefore, we  
calculated PA by three methods, starting with a simple approach based on the standard deviations (SD) of the records that is  
independent of stratigraphic correlations, and then subsequently based on correlations of recorded global exogenic variability  
130 in stable carbon isotope ratios, which finally is finetuned using paleothermometry to test the robustness of the obtained PA  
factors (see Supplement, Section 2).



## 2.2 Calcareous nannofossils

We analyzed 76 additional samples from Site 959D Cores 41R–35R for calcareous nannofossil assemblages. For this, <1 g was mixed from which an aliquot was analyzed at Padova University, Italy. For optimal constraints, 31 samples were taken  
135 from Core 39R, achieving an average sample spacing of 22 cm. Calcareous nannofossil zonation follows Agnini et al., (2014) and ages were calculated utilizing the astronomically calibrated magnetochron ages of Westerhold et al. (2017).

## 2.3 Bulk sediment analysis

Sampled intervals across cores 41R to 38R were analyzed for bulk sedimentary characteristics to provide, complementary to the calcareous nannofossil biostratigraphy, a chemostratigraphic framework of the early Eocene interval of Site 959. The bulk  
140 sediment measurements include magnetic susceptibility (MS), bulk carbonate stable carbon ( $\delta^{13}\text{C}$ ) and oxygen ( $\delta^{18}\text{O}$ ) isotope ratios, total organic carbon (TOC) content, organic matter stable carbon isotope ratios ( $\delta^{13}\text{C}_{\text{org}}$ ) and weight percentage calcium carbonate ( $\text{CaCO}_3\text{wt}\%$ ).

### 2.3.1 Magnetic Susceptibility

Bulk MS, a measure for the relative abundance of magnetic (mostly Fe-rich) minerals, was measured on 904 samples. The  
145 samples were weighed and put in plastic 40 ml beakers. The measurements were carried out with a MFK1-FA Multifunction Kappabridge. The values of bulk MS are reported in  $\chi$ . Analytical precision, determined by the SD of replicate measurements, was better than  $5 * 10^{-10} \chi$ .

### 2.3.2 Carbonate oxygen and carbon isotopes

Bulk carbonate isotopes were measured to trace (stratigraphically relevant)  $\delta^{13}\text{C}$  variations of surface ocean dissolved inorganic  
150 carbon (DIC) and potentially trace temperature-forced  $\delta^{18}\text{O}$  variations of biogenic carbonate. For 828 samples, between 100 and 2200  $\mu\text{g}$  of powdered sediment was analyzed on a Thermo Finnigan GasBench II system, coupled to a Thermo Delta-V mass spectrometer. Isotope values were calibrated to an in-house carbonate standard `NAXOS` and international standard `IAEA-CO-1`. All isotope values are reported against Vienna Pee Dee Belemnite (VPDB). Analytical precision, as determined by the SD of the in-house standard was better than 0.07‰ for  $\delta^{18}\text{O}$  and 0.07‰  $\delta^{13}\text{C}$ . For each sample, the  $\text{CaCO}_3\text{wt}\%$  was  
155 estimated by comparing the signal-to-mass ratio to that of the pure carbonate standards. Precision of this method was better than 13 %, based on the SD of the standards.

### 2.3.3 Organic carbon isotopes and content

A selection of 400 samples were analyzed for  $\delta^{13}\text{C}_{\text{org}}$ , which in addition to the inorganic  $\delta^{13}\text{C}$  was used for carbon isotope  
160 stratigraphy. For this, first 0.3 g of powdered sample was weighed in a 25 ml plastic Greiner tube and treated with 15 ml of 1 M HCl to remove carbonates. The samples were washed with UHQ and dried in an oven for 62 hours at 60 °C. Approximately



15 mg of dried and homogenized residue was used to determine TOC content with a Fisons CNS analyzer. Bulk total organic carbon isotope ratios were measured with a Finnigan DELTA plus IRMS, coupled to the Fisons elemental analyzer. Isotope values were calibrated against inhouse standards nicotinamide and 'GQ' and reported against VPDB. Precision was determined by the SD of the GQ standard and arrived at better than 0.04 ‰  $\delta^{13}\text{C}$  and 0.07 % for TOC content. Sample weights before and after decalcification were compared to provide an additional estimate of  $\text{CaCO}_3$ wt%.

## 2.4 Lipid biomarkers

### 2.4.1 GDGT analysis

To reconstruct SST variability at Site 959, we applied  $\text{TEX}_{86}$ , a lipid biomarker proxy based on the temperature-regulated homeoviscous adaptation of Thaumarcheotal cell membrane lipids (glycerol dialkyl glycerol tetraethers; GDGTs) (Schouten et al., 2002). For the analysis of GDGTs, between 3 and 45 g of sediment of 268 samples was powdered and weighed in glass tubes. Due to low GDGT concentrations in some intervals ( $<0.1$  ng/g), some neighboring samples were pooled up to a maximum of 125 g of sediment. Lipids were extracted in a 25 ml solvent mixture of dichloromethane (DCM):methanol (MeOH) (9:1 by volume:volume) by a Milestone Ethos X Microwave Extraction System, set to 70 °C for 50 minutes. Lipid extracts were filtered over a  $\text{NaSO}_4$  columns and dried under a  $\text{N}_2$  blower. The dry lipid extracts were separated in apolar, neutral and polar fractions through  $\text{AlO}_x$  column chromatography, with hexane/DCM (9:1), hexane:DCM (1:1) and 1:1 DCM:MeOH (1:1), respectively as mobile phases. Fractions were again dried under a  $\text{N}_2$  blower and weighed. To the polar fractions, 99 ng of a  $\text{C}_{46}$  GTGT standard was added to enable quantitative analysis. Polar fractions were diluted in hexane/isopropanol (99:1) to a concentration of 2 mg/ml, and pressed through a 0.45  $\mu\text{m}$  polytetrafluoroethylene filter into a 1 ml glass vial. Per sample, 10  $\mu\text{l}$  filtered polar fraction was analyzed by an Agilent 1290 infinity ultra high-performance liquid chromatography (UHPLC) coupled to an Agilent 6135 single quadrupole mass spectrometer with settings according to (Hopmans et al., 2016). Measurements were considered below proper detection limits for application of  $\text{TEX}_{86}$  when one or more isoprenoid GDGT peaks did not exceed three times background noise (i.e., peak areas below  $\sim 2000$  units). This resulted in exclusion of 47 samples.

Analytical precision was estimated by analysis of a systematically injected in-house GDGT standard, which resulted in a SD of 0.006  $\text{TEX}_{86}$  units, corresponding with 0.2 °C (using the  $\text{TEX}_{86}^{\text{H}}$  calibration (Kim et al., 2010)) in the  $\text{TEX}_{86}$  range of early Eocene Site 959. This error represents the analytical error of temperature variability estimates, which is relevant for PA calculations, so any recorded variability with larger magnitude implies a climatological signal. Robustness of applying this standard-based analytical uncertainty to our dataset was confirmed by repeated measurements ( $n = 9$ ) of one sample, which resulted in a SD of 0.12 °C ( $\text{TEX}_{86}^{\text{H}}$ ).



## 190 2.4.2 Indices for confounding factors

Multiple GDGT-ratios were examined to assess confounding factors on the  $\text{TEX}_{86}$ , by testing for contribution of GDGTs from terrestrial sources (Hopmans et al., 2004), methanogens (Blaga et al., 2009), anaerobic methane oxidizers (Weijers et al., 2011), methanotrophs (Zhang et al., 2011) and deep-water communities (Taylor et al., 2013b), and check for non-thermal influence on the crenarchaeol isomer (O'Brien et al., 2017) and other non-thermal factors (Zhang et al., 2016) using the R-script by Bijl et al. (2021) (Supplement, Fig. S2). Two samples were left out of further analysis based on their GDGT-2/GDGT-3 ratio, a measure for deep water contribution, exceeding threshold values of 5 (Taylor et al., 2013b; Rattanasriampaipong et al., 2022). Furthermore, we left out four samples based on a deviation of the expected Ring Index values relative to their  $\text{TEX}_{86}$  value ( $\Delta$ -RI) (Zhang et al., 2016), which are positioned throughout the studied interval, but exhibit no apparent pattern with other geochemical records. All other samples are well within the ranges of the modern calibration dataset and are therefore deemed suitable for temperature reconstruction, resulting in a final dataset of 216 datapoints with near-continuous stratigraphic coverage across Core 39R.

## 2.4.3 $\text{TEX}_{86}$ calibration

Tropical Eocene  $\text{TEX}_{86}$  values exceed modern surface sediment values. Moreover, Thaumarchaeotal GDGTs in marine sediments originate not from within, but dominantly from just below the ocean surface mixed layer (Massana et al., 2000; Karner et al., 2001; Sinninghe Damsté et al., 2002; Wuchter et al., 2006; Hurley et al., 2018; Besseling et al., 2019; van der Weijst et al., 2022). These issues imply uncertainty regarding the  $\text{TEX}_{86}$ -SST relationship. To account for this uncertainty, we converted our  $\text{TEX}_{86}$  record to temperature using calibrations for both SST ( $\text{TEX}_{86}^{\text{H}}$ ) (Kim et al., 2010) and a shallow subsurface (100–250 m water depth) temperature (SubT) from Ho and Laepple (2016), that together cover the plausible range of  $\text{TEX}_{86}$ -SST relationships (see Supplement Section 1 for discussion). Importantly, as shallow SubT variability equals SST variability (Supplement, Fig. S1b), this approach provides an error range for assessing tropical SST variability.

## 2.5 Palynology

To evaluate the influence of local or regional environmental factors (e.g., upwelling, terrestrial input) on temperature variability at Site 959, we analyzed palynological assemblages throughout Core 39R. Specifically, we analyzed fossil dinoflagellate cysts (dinocysts) assemblages, which have proven to be sensitive recorders of Paleogene surface water conditions (Sluijs et al., 2005; Frieling and Sluijs, 2018). For palynological preparation, of 82 samples, 5–10 g of freeze-dried sediment were crushed to ~2 mm chunks. A tablet containing a known amount of *Lycopodium clavatum* spores was added to enable quantitative analysis of organic microfossils (Stockmarr, 1972). Samples were treated with 10 % HCl and decanted to remove carbonates. Next, silicates were removed by repeated treatment with 40 % HF and 30 % HCl and subsequent decantation after each step. Residues were neutralized with tap water and sieved between 250- $\mu\text{m}$  and 15- $\mu\text{m}$  meshes to obtain the required particle size. Palynological residues were mounted on microscope slides by mixing one drop of concentrated, homogenized, residue with



glycerin jelly, and covering it with a cover glass. Palynological analysis of dinocysts was performed under 400x magnification until 200 dinocysts were counted, or no material was left.

### 3. Results

#### 3.1 Refined stratigraphic framework

225 Previous work constructed a low-resolution age model for the Eocene interval of Site 959 using  $^{187}\text{Os}/^{188}\text{Os}$ ,  $\delta^{13}\text{C}$  and calcareous nannofossils, supported by the identification of Milankovitch cyclicity in sediment color (Cramwinckel et al., 2018). We here amended the age model for the lower Eocene interval based on higher resolution calcareous nannofossil biostratigraphy. We pair the new biostratigraphic constraints with bulk organic carbon and bulk carbonate  $\delta^{13}\text{C}$  stratigraphy in a combined age model. This is subsequently used to correlate to global exogenic trends recorded in deep ocean benthic  
230 foraminifer isotope stratigraphy (Westerhold et al., 2020).

Our calcareous nannofossil biostratigraphic analysis indicates the same position for the Base of *Tribraichiatius orthostylus* and Top of *T. contortus* in the top interval of Core 40R at 785.05( $\pm$ 0.38) mbsf. Despite the rare presence and poor preservation of calcareous nannofossils in the interval of ~777–778 mbsf, the base of *Discoaster lodoensis* is recorded at 777.84( $\pm$ 0.12) mbsf, previously found to occur just before the K event (Agnini et al., 2009). The Top of *T. orthostylus*, generally found to occur  
235 close to the R event (Westerhold et al., 2017), is positioned in the ~9 m core gap above Core 39R.

The calcareous nannofossil biostratigraphy allows correlation of the  $\delta^{13}\text{C}$  records to long-term trends and short-term carbon cycle perturbations captured in the orbitally tuned benthic foraminifer isotope records (Westerhold et al., 2020), which reflect global exogenic carbon cycle trends (Fig. 1). A gradual decline in bulk carbonate  $\delta^{13}\text{C}$  between 800 and 784 mbsf (Cores 41R, 40R) corresponds to calcareous nannofossil assemblage zones of CNE2 up to the boundary with CNE3 (~55.6–54.3 Ma),  
240 following global deep ocean isotope trends (Westerhold et al., 2020). The small stratigraphic interval covered by Core 38R (765.09–764.25 mbsf), positioned within Zone CNE5 (~50.6–48.9 Ma), again displays higher  $\delta^{13}\text{C}$  values, which is also consistent with the long-term trend captured in the benthic carbon isotopes.

Several negative CIEs are recorded in both carbonate and bulk organic  $\delta^{13}\text{C}$  records in Core 39R (Fig. 1, Fig. 2a). These CIEs typically coincide with drops in  $\text{CaCO}_3\text{wt}\%$  and peaks in magnetic susceptibility, consistent with other deep ocean records of  
245 early Eocene events. However, the very low bulk carbonate  $\delta^{18}\text{O}$  and  $\delta^{13}\text{C}$  values ( $\delta^{13}\text{C}$  down to -6.12 ‰), and their strong correlation, and overall low  $\text{CaCO}_3\text{wt}\%$  (Supplement, Fig. S3) likely relate to an authigenic carbonate component in the sediment of 39R–38R, consistent with porewater analyses (Masclé et al., 1996; Zachos et al., 2010; Leon-Rodriguez and Dickens, 2010; Slotnick et al., 2012), which compromises reconstruction of absolute values and the degree of variability of surface DIC variations. It is therefore unlikely that the large magnitude of recorded bulk carbonate  $\delta^{13}\text{C}$  excursions (here in  
250 the order of 2–4 ‰) represents  $\delta^{13}\text{C}$ -DIC variability in the surface ocean. The congruence between the major  $\delta^{13}\text{C}_{\text{org}}$  and carbonate  $\delta^{13}\text{C}$  excursions implies, however, that the stratigraphic positions of CIEs are still recorded in the isotopic signal of the carbonate. Due to the diagenetic overprinting the bulk carbonate  $\delta^{18}\text{O}$  record is not further considered as climate signal.





Based on the biostratigraphic boundary of CNE3-CNE4 (~52.9 Ma) at ~777.8 mbsf, the negative CIE at 777.5 mbsf can be identified as the K event (also called ‘ETM-3’ or ‘X’). As the CNE2-CNE3 boundary in the top of Core 40R just predates the H1 (‘ETM-2’) and H2 CIE events, these events are likely to be positioned in the ~2.6 m core gap between Core 40R and 39R. The identification of other carbon cycle events can subsequently be inferred using the positions of the CIEs and interpolation between established bio- and chemostratigraphy. Our combined stratigraphic constraints (Fig. 1) show that the recorded negative CIEs at Site 959 represent at least five globally recognized CIEs: I1, I2, J, K and L. Note that we correlate two excursions related to L, here termed L1 and L2, while these events were previously not separated (Westerhold et al., 2018; Lauretano et al., 2018). This study's age model, including the biostratigraphic and carbon isotope stratigraphic tie-points, is available on Zenodo (DOI: 10.5281/zenodo.8309643).

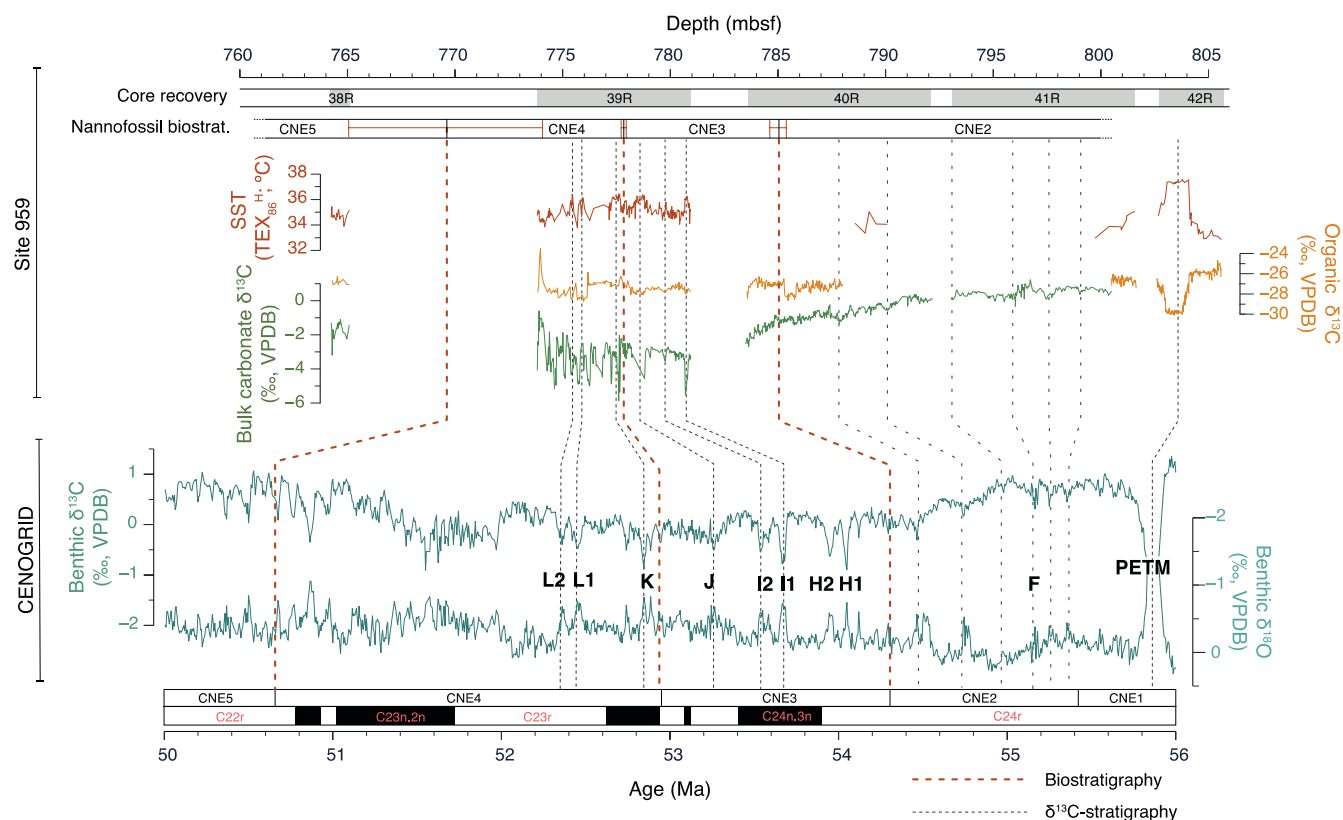


**Figure 1.** Stratigraphic correlation between Site 959 Cores 38R–42R and the CENOGRID benthic compilation. Top of figure: Site 959 data (Cramwinckel et al., 2018; Frieling et al., 2019; This Study) with Core recovery, nannofossil biostratigraphic zonation (with associated depth uncertainty), TEX<sub>86</sub>, bulk organic δ<sup>13</sup>C and bulk carbonate δ<sup>13</sup>C against depth. Bottom part of figure: benthic δ<sup>13</sup>C and δ<sup>18</sup>O from the CENOGRID (Westerhold et al., 2020). Grey dashed lines indicate correlations based on carbon isotope ratios; red dashed lines indicate biostratigraphic correlations.

270



### 3.2 TEX<sub>86</sub>

Our new TEX<sub>86</sub>-based SST record, with a median resolution of ~4 kyr across Core 39R, indicates average values of 35.2±0.6 °C following the TEX<sub>86</sub><sup>H</sup> calibration (see Supplement Section 1). A ~0.7 °C long-term warming marks the lower part of the record up to ~777 mbsf, after which values drop by ~1 °C towards ~774 mbsf (Fig. 2). Absolute SSTs derived from one single proxy, including TEX<sub>86</sub>, should be taken with care (see Supplement, Section 1), but our new SSTs match the previously established early Eocene range of tropical-band SSTs based on δ<sup>18</sup>O, clumped isotopes and Mg/Ca paleothermometry of glassy

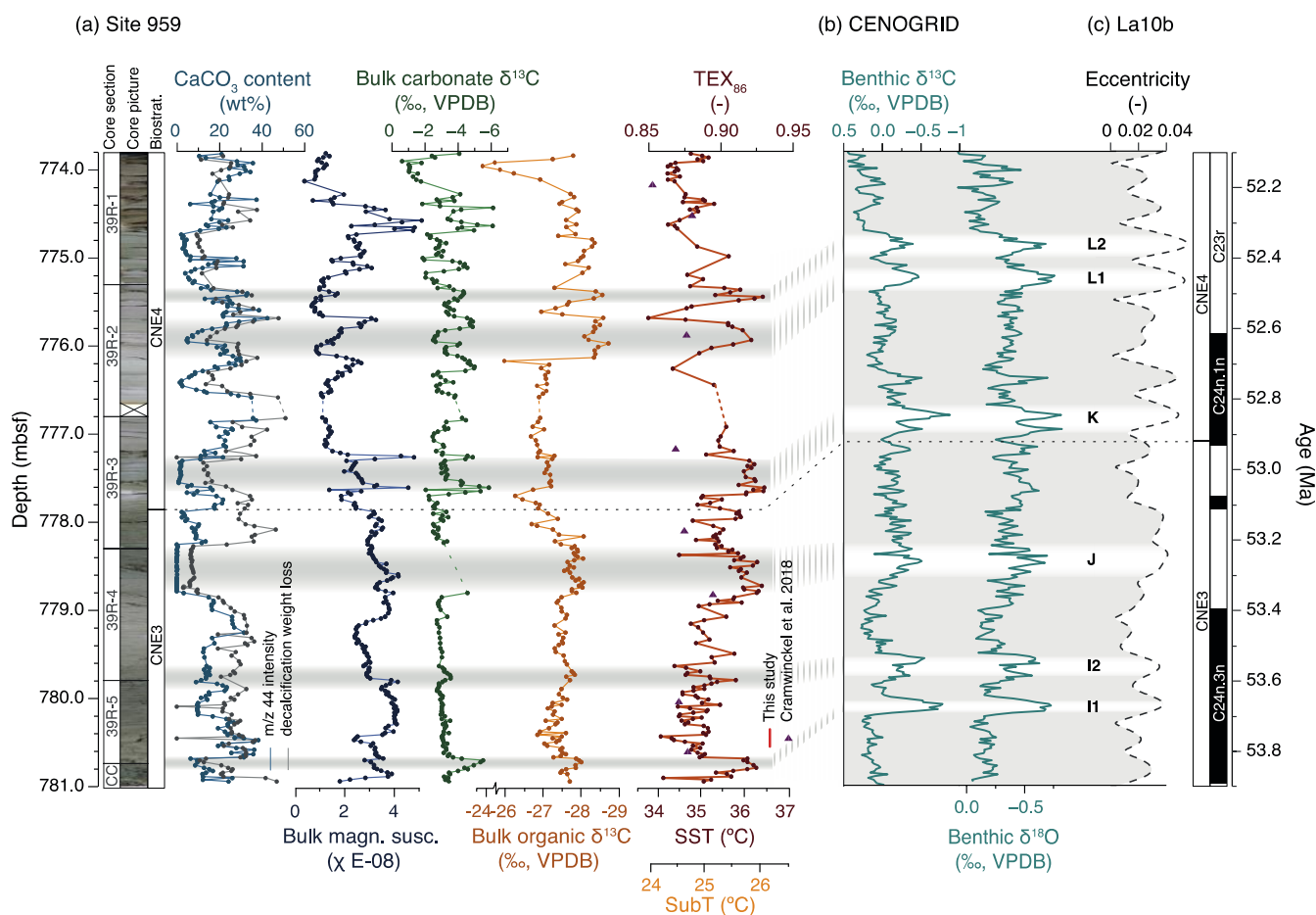


**Figure 2.** Downcore results of Site 959 Core 39R and correlation to benthic records and astronomical solution. (a) Results from Site 959 Core 39R against depth in mbsf. From left to right: core photographs (Masle et al., 1996), calcareous nannofossil biostratigraphy (follows zonation by Agnini et al. (2014)), CaCO<sub>3</sub> content estimated from signal intensity during isotope ratio mass spectrometry analyses of bulk sediment (blue) and sediment weight loss after decalcification (grey), bulk MS, bulk carbonate δ<sup>13</sup>C, bulk organic δ<sup>13</sup>C and TEX<sub>86</sub>. The 8 pre-existing TEX<sub>86</sub> data of Cramwinckel et al. (2018) are shown in purple triangles. Horizontal bars indicate interpreted CIE horizons. (b) Deep ocean benthic foraminifer δ<sup>13</sup>C and δ<sup>18</sup>O from the CENOGRID compilation (Westerhold et al., 2020). Calcareous nannofossil zones of Agnini et al. (2014) and CIEs I1, I2, J, K, L1 and L2 are astronomically calibrated (Westerhold et al., 2017) to the La10b astronomical solution (Laskar et al., 2011) (c).



foraminifera and  $\text{TEX}_{86}$  (Evans et al., 2018; Cramwinckel et al., 2018; Gaskell et al., 2022). Our SST results are, however, generally higher compared to a previous  $\text{TEX}_{86}$  study of the same Site (Fig. 2) (Cramwinckel et al., 2018). We attribute this offset to a sampling bias, as their analyses predominantly targeted darker sediment intervals for optimal GDGT preservation. Our data now reveal that the darker intervals often coincide with slightly lower  $\text{TEX}_{86}$  values (e.g., at  $\sim 778.2$  and  $\sim 774.1$ ; Fig. 2).

The records shows pronounced variability on orbital time scales, including warming across the various CIEs. As palynological analysis indicates an open ocean setting, slightly more oligotrophic than the remainder of the Eocene (Cramwinckel et al., 2018), without regional environmental variations (e.g., upwelling or terrestrial input) that would influence SSTs (Supplement, Fig. S4), we assume that this reconstructed SST variability at Site 959 tracks the variability of the complete tropical band, in agreement with model simulations (Supplement, Fig. 1a).

### 3.3 Ice-free polar amplification of orbital-scale climate variability

We first approximate short-term PA independently of direct stratigraphic correlation by a comparison of the SD of both records, after detrending the dataset to remove Myr-scale trends. Over the interval of  $\sim 53.8$ – $52$  Ma, the SDs of the detrended BWT record is  $0.7$  °C versus  $0.5$  °C of our tropical SSTs, suggesting that BWT variability was approximately amplified with a factor  $\sim 1.4$  with respect to the equatorial SSTs (Fig. 3a). Naturally, this simple approach is sensitive to the different analytical errors of the temperature proxies. The analytical errors ( $\sim 0.2$  °C for SST (see Methods) and  $\sim 0.4$  °C for  $\delta^{18}\text{O}$ -BWT (see Supplement, Section 2) are, however, too small to explain the complete offset in variability of the two records, suggesting that the obtained value is a crude approximation of PA. Performing the same exercise with SubT-calibrated  $\text{TEX}_{86}$  data yields a SD of  $0.4$  °C, and subsequently a higher amplification factor of  $\sim 1.8$ . Note that the higher PA estimate from SubT relative to SST does not imply that temperature variability was amplified more in the subsurface than in the surface ocean. Rather, calibrating equatorial  $\text{TEX}_{86}$  values to a modern subsurface dataset yields a subdued  $\text{TEX}_{86}$ -temperature relation and therefore a lower reconstructed amplitude of past tropical temperature variability.

Next, we compare the magnitude of the recorded warming across negative CIEs, relative to the million-year background trend, between the tropics and deep sea (Fig. 3a–b). In comparison to deep ocean warming, events I1–L2 show a dampened response in the tropics. The dampened magnitude of tropical warming can be quantified as PA of climate change, with an amplification factor of  $1.8 \pm 0.2$  (SubT =  $2.4 \pm 0.3$ ). This amplification factor demonstrates that warming during these events was indeed amplified in the Southern Ocean surface waters, the presumed origin of early Eocene bottom waters, with respect to the tropical surface ocean. We compare these PA values to the PETM estimates, for which we use averaged previously published estimates on equatorial surface warming ( $\Delta T = 2.9 \pm 0.5$  °C) (Frieling et al., 2017, 2019) and BWT reconstructions ( $\Delta T = 5.4 \pm 0.5$  °C) (Dunkley Jones et al., 2013) (Fig. 2b). Importantly, the estimates for the PETM fall within the projected regression line of events I1–L2, which indicates that, while the PETM was a more severe event in terms of climate change, PA was similar to the smaller events.

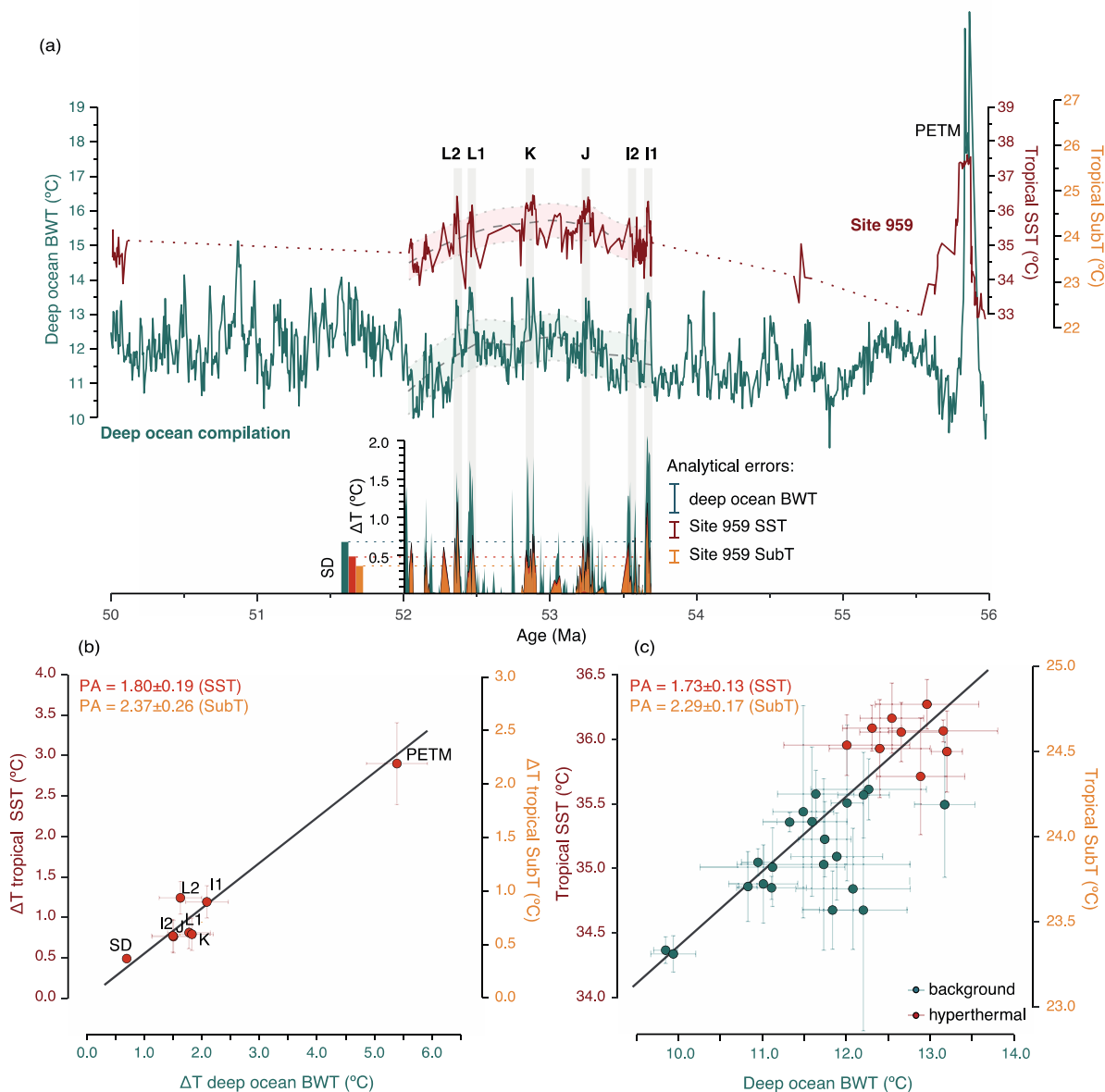


**Figure 3.** Comparison of temperature variability in the tropical (sub)surface and the deep ocean during the early Eocene. **(a)** Comparison of SST/SubT from Site 959 (red) and the CENOGRID benthic compilation (Westerhold et al., 2020) (green) (see Supplement, Section 2, for BWT calculations). The colored bands indicate the LOESS filter (window = 1 Myr) and 1 SD. Positive temperature deviations of deep ocean BWT (green), tropical SubT (yellow) and SST (red) relative to the 1-Myr trend are indicated below. CIEs are marked with their respective names above the record. Bars on the left indicate the values of SD per dataset, analytical errors are indicated on the right. **(b)** Magnitude of SST/SubT rise versus BWT rise across the multiple hyperthermals depicted in panel (a) (SST on left axis, SubT on right axis) and SD of the records as in bottom left panel (a). The errors (crosses) reflect analytical errors. The PETM data is from literature (Dunkley Jones et al., 2013; Frieling et al., 2017, 2019) with error crosses indicate standard error of combined estimates. The regression is only based on the warming of hyperthermals I1–L2. **(c)** Short-term, 20-kyr-binned Site 959 temperature dataset versus BWTs (Westerhold et al., 2020). The black lines in panels (b) and (c) represent the Deming regression lines between equatorial (sub)SSTs and BWTs, with respective PA factors on top left of the panels.



Our  $\text{TEX}_{86}$  record varies in concert with the deep ocean BWT record (Westerhold et al., 2020) (Fig. 3) and shows that sub-million-year timescale climate variability was not limited to the globally recognized CIEs. Polar amplification of the complete, eccentricity-scale climate variability, was evaluated by directly matching the SST record to the BWT record and dividing both records in 20-kyr bins (see Supplement, Section 2). For this detailed correlation, we included minor finetuning between related features in the benthic  $\delta^{18}\text{O}$  record and  $\text{TEX}_{86}$  records, so that warming events optimally line up (e.g., peak SSTs are compared to peak BWTs) (Fig. S7c). Clearly, all other correlations are based on biostratigraphy and carbon isotope stratigraphy and therefore the positive relation between surface and deep ocean temperature variability is emergent. This observation warrants the additional correlations made here for the regression analysis on eccentricity scale to quantify polar amplification, but it assumes correspondence in the timing between surface and deep ocean temperature variability. A Deming regression using the binned data indicates a PA factor of  $\sim 1.7 \pm 0.1$  ( $\text{SubT} = 2.3 \pm 0.2$ ) between  $\sim 54$  and  $\sim 52$  Ma (Fig. 3c). Specifically, the PA derived from the short timespan included in the data bins demonstrates that climate change forced by 100-kyr eccentricity was amplified in the Southern Ocean during an ice-free climate state.

## 4. Discussion

### 4.1 I1, I2, J, K, L1 and L2 are hyperthermal events

The horizons of CIE events I1, I2, J, K, L1 and L2 all coincide with transient sea surface warming at Site 959, with a magnitude of approximately  $\sim 1$  °C ( $\sim 0.7$  °C SubT). Hence, the observed link between transient warming reconstructed in the tropics and deep ocean, together with the coeval deep ocean carbonate dissolution horizons (Leon-Rodriguez and Dickens, 2010; Westerhold et al., 2017), presents conclusive evidence that all these orbitally triggered carbon cycle perturbations were transient global warming events. As previously hypothesized (e.g., Cramer et al., 2003; Lourens et al., 2005), combined with the occurrence of CIEs and deep ocean carbonate dissolution, this evidence of global warming now proves that orbital forcing led to variability in atmospheric  $p\text{CO}_2$  during the early Eocene ice-free world, due to carbon cycle feedbacks (e.g., Dickens, 2001).

### 4.2 Polar amplification during the ice-free EECO

Our reconstructed short-term (20-kyr) PA factor of 1.7–2.3 lies close to previous estimates on much longer, million-year timescales during a similar hothouse climate (Cramwinckel et al., 2018; Gaskell et al., 2022). To provide a more thorough comparison with  $10^6$ -year timescale PA, we combine our high-resolution dataset with previously published late Paleocene–early Oligocene  $\text{TEX}_{86}$ -based SST data from Site 959 (Cramwinckel et al., 2018; Frieling et al., 2019) and compare to the deep ocean BWT dataset (Westerhold et al., 2020) in 1-Myr bins (Fig. 4a, yellow line). Remarkably, this 1-Myr-binned analysis results in a low to absent PA ( $\sim 1.2 \pm 0.1$ ) across the long-term Eocene cooling trend, that clearly differs from the 20-kyr-binned PA result during the early Eocene hyperthermals (Fig. 4a, red line). The small offset between our reconstructed SSTs and that of Cramwinckel et al. (2018) ( $\sim 1$  °C, Fig. 2) is insufficient to explain this difference in PA factors, especially as both datasets



are combined for the long-term PA estimate in Fig. 4a. The discrepancy between long- and short-term PA could point to a timescale dependent PA, or alternatively to a (non-linear) GMST-dependent PA, as our short-term data is concentrated in the high temperature end. However, a change of local oceanographic conditions at Site 959 is a more likely explanation for the low PA in the long-term Site 959 PA estimate. Contrary to our high-resolution early Eocene interval (~54-52 Ma) (Supplement, Fig. S4), dinoflagellate cysts produced by heterotrophic taxa appear in the record around 49 Ma (Cramwinckel et al., 2018). In combination with the coeval increase in TOC, we interpret this as a progressive increase of surface water productivity at the Gulf of Guinea during the Eocene relative to the here-studied interval. At this location, increased productivity most likely relates to increased (seasonal) upwelling of cooler, nutrient-rich, sub-thermocline waters. Based on their records, Cramwinckel et al. (2018) assumed the presence of constant upwelling between ~58 and ~40 Ma at Site 959. However, specifically in the here studied interval (~54–52 Ma), we find no evidence for upwelling in the dinocyst assemblages and this should have diminished the cooling of surface waters resulting in the higher temperatures we record in the early Eocene. This amplifies the apparent long-term cooling from the early to middle Eocene relative to the estimates of Cramwinckel et al. (2018), and reduces apparent PA. We therefore attribute the stronger cooling than Cramwinckel et al. (2018) recorded from the early to middle Eocene to reflect increased upwelling starting around 49 Ma. To reduce the effect of local cooling on reconstructed long-term PA, we compare our short-term analysis to a long-term PA estimate that utilizes a more comprehensive tropical SST data compilation (Cramwinckel et al., 2018; Gaskell et al., 2022), including  $\text{TEX}_{86}$ ,  $\delta^{18}\text{O}$ , Mg/Ca and  $\Delta_{47}$  proxy records of 16 locations, to which we add our new dataset. A 1-Myr-binned comparison between this tropical SST compilation and deep ocean BWTs (Westerhold et al., 2020) results in a PA factor of  $\sim 1.6 \pm 0.1$  (Fig. 4a, green line), which is within error of our short-term PA estimate. Coherence between the short- and long-term PA estimates implies that PA of the long-term  $10^6$ – $10^7$ -year stochastic climate trends of the entire largely ice-free Eocene is equal to PA on  $10^4$ -year climate variability of the early Eocene. Additionally, this correspondence implies that Eocene PA was not impacted by feedback mechanisms that act on  $10^4$ -year timescales or longer. To test the capability of fully coupled climate models to accurately project ice-free PA, we compare our proxy-based estimates of PA to the DeepMIP simulations (Lunt et al., 2021). For optimal comparison, we use modelled low-latitude ( $<30^\circ$ ) annually averaged SSTs versus high-latitude Southern Ocean ( $>60^\circ$ ) winter average SSTs, the dominant source of Eocene bottom waters in these simulations, consistent with reconstructions (Fig. 4a, grey line). The magnitude of combined-model-derived PA is  $\sim 1.2$  and only small differences exist between individual model PA results, with highest PA value recorded by GFDL (PA =  $\sim 1.3$ ) and smallest by COSMOS (PA =  $\sim 1.1$ ). Utilization of tropical SSTs resulting from the  $\text{TEX}_{86}^{\text{H}}$ -SST calibration, which we consider to provide the most realistic SST calibration in our range of  $\text{TEX}_{86}$  values (Supplement, Section 1), shows the best correspondence of short-term PA with PA from the model simulations, while using a SubT calibration results in larger PA factors. In contrast to the here used exponential calibrations, linear  $\text{TEX}_{86}$  calibrations lead to much higher reconstructed tropical SST variability and consequently an absent or even negative PA factor.

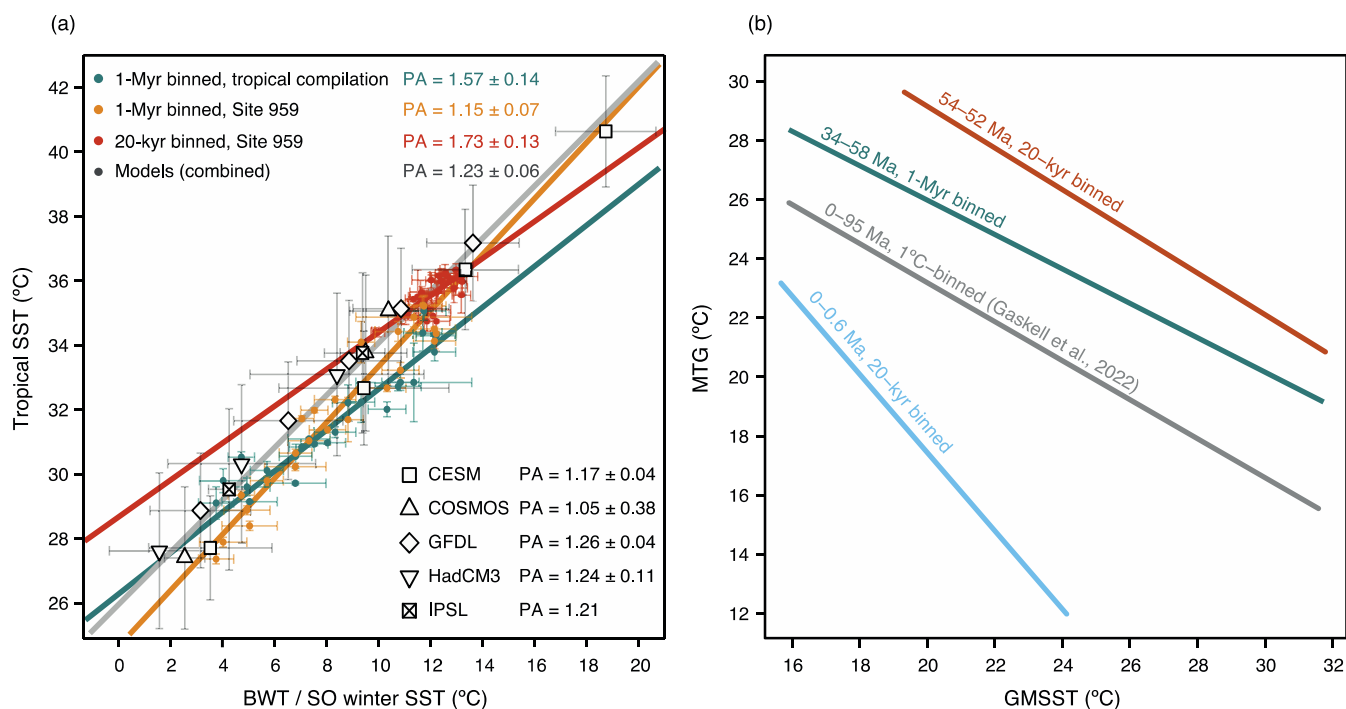


**Figure 4.** Polar amplification (a) and global mean sea surface temperature *versus* meridional temperature gradient (b) of various datasets and timespans. (a) Comparison of long-term (1-Myr bins), short-term (20-kyr bins) and modeled PA. In green, the 1-Myr binned tropical SST data compilation (Cramwinckel et al., 2018; Gaskell et al., 2022; This Study) versus CENOGRID (Westerhold et al., 2020) BWTs, in yellow the 1-Myr binned complete Eocene Site 959 TEX<sub>86</sub>-based SSTs (Cramwinckel et al., 2018; Frieling et al., 2019; This Study) versus the CENOGRID BWTs and in red the 20-kyr binned Site 959 TEX<sub>86</sub>-based SSTs versus the CENOGRID (as in Fig. 3c). Colored crosses represent uncertainty intervals based on binning (1 standard error). In grey, model output from a selection of different model simulations compiled from Lunt et al. (2021) (see Supplement, Section 2). Uncertainty crosses in the model datapoints represent one standard deviation across the selected latitudinal bands. All solid lines depict Deming regressions, based on the binned data and abovementioned uncertainty intervals. (b) GMSST versus  $\Delta T$  Deming regression lines as calculated from 20-kyr binning between 54 and 52 Ma of Site 959 and CENOGRID (red), 1-Myr binning of tropical SST compilation and CENOGRID (green), temperature (1 °C) binning between high and low-latitude  $\delta^{18}\text{O}$  data from 0 to 95 Ma (Gaskell et al., 2022) (grey) and 20-kyr binning the tropical (Herbert et al., 2010) and high-latitude (Lawrence et al., 2009; Martínez-García et al., 2010; Ho et al., 2012) SST datasets from 0 to 0.6 Ma (blue).

The PA factor of the DeepMIP models represents the non-ice-albedo PA of state-of-the art climate models. Therefore, the  
 375 general agreement between our results and the magnitude of PA expressed by the DeepMIP output implies that (atmospheric)  
 feedback processes to greenhouse gas forcing seem to be adequately represented in the DeepMIP model suite. However, our  
 reconstruction points to somewhat larger PA in an ice-free world than that in the models, suggesting that the non-ice-related  
 factors, such as hydrological feedbacks, might be underestimated in IPCC class current-generation fully coupled climate  
 models. This is consistent with the commonly found result that many models underpredict Eocene PA and overestimate the  
 380 MTGs. Consequently, the models seem to underestimate the non-ice related, hydrological component of polar amplification.



### 4.3 Eccentricity-forced global mean sea surface temperature

Our combined dataset of tropical SST and open ocean BWT approximates the range of warmest and coldest temperatures of the Eocene ocean, and can be utilized to estimate variations in both global mean sea surface temperature (GMSST) and MTG, by an area weighted average and the difference between tropical SST and BWT, respectively (Caballero and Huber, 2013; 385 Gaskell et al., 2022). Intriguingly, the slope of the relationship between the MTG and GMSST is comparable between the 20-kyr binned dataset, the Myr-binned dataset and the  $\delta^{18}\text{O}$ -based data compilation from Gaskell et al. (2022) (Fig. 3b). Absolute GMSSTs are, however, offset by  $\sim 2$  °C between our record and the Gaskell et al. (2022) dataset, likely due the different nature of the datasets, including general discrepancies in published  $\delta^{18}\text{O}$  records, inclusion of different sites, calibrations, and isotopic corrections (Supplement, Fig. S5).

390 Finally, we assess GMSST variability on eccentricity timescales (Fig. 4b, 5). Our analysis indicates that GMSST variability of recorded hyperthermals is  $\sim 1\text{--}1.5$  °C (using  $\text{TEX}_{86}^{\text{H}}$ ) (Fig. 5a), which reveals that the modern GMSST warming of  $\sim 1$  °C is already in the range of the early Eocene hyperthermal events. Importantly, we also record up to 0.7 °C variability on an approximate 100-kyr-eccentricity timescale in periods outside of previously declared CIEs (e.g., at  $\sim 53.0$  and  $\sim 52.2$  Ma in Fig 5a). However, we note that some of our correlations between the tropical SST variations and the deep-ocean based on bio- and 395 chemostratigraphy were finetuned using temperature proxies (Supplement, Section 1), which might yield erroneous correlations of local temperature variations. Nevertheless, if observed GMSST variability indeed presents (100-kyr) eccentricity-paced global temperature variation, the Eocene ice-free climate may have responded strongly to small ( $\sim 0.5$  W/m<sup>2</sup>) variation in global incoming solar radiation. This is strongly reminiscent of Pleistocene glacial-interglacial cycles (Herbert et al., 2010; Martínez-García et al., 2010; Ho et al., 2012), but in the absence of strong amplifying ice and snow albedo feedbacks.

400 This implies, as suggested by previous work (Vervoort et al., 2021), a sensitive carbon cycle feedback mechanism at play during the early Eocene. Although the exact mechanisms are uncertain, we note that this feedback must be strong, because the logarithmic relation between CO<sub>2</sub> forcing and global mean temperature requires large volumes of CO<sub>2</sub> to force global temperature in the early Eocene high-CO<sub>2</sub> state (e.g., Lunt et al., 2021). A back-of-the-envelope calculation indicates that, given an averaged modeled early Eocene Equilibrium Climate Sensitivity of 4.5 °C per  $p\text{CO}_2$  doubling (Lunt et al., 2021) and





405 reconstructed background CO<sub>2</sub> concentrations of approximately ~1470 ppm (Anagnostou et al., 2020), recorded temperature  
 variability would require a forcing of ~245 ppm CO<sub>2</sub> for the hyperthermals ( $\Delta T = 1.0$  °C) and ~118 ppm CO<sub>2</sub> for the other  
 eccentricity-forced warmings ( $\Delta T = 0.5$  °C), broadly in line with previous estimates based on carbonate chemistry (Zeebe et  
 al., 2017).

By means of comparison, we perform an additional GMSST estimate in terms of sampling and calculations for the most recent  
 410 orbitally forced global temperature variations, which consist of the last few glacial-interglacial cycles (Fig. 5b). This dataset,  
 composed of U<sup>K</sup><sub>37</sub> data from tropics (Herbert et al., 2010) and mid to high latitudes (Lawrence et al., 2009; Martínez-García et  
 al., 2010; Ho et al., 2012) shows GMSST variations of ~4 °C, similar to a recent estimate (Annan et al., 2022), as well as a

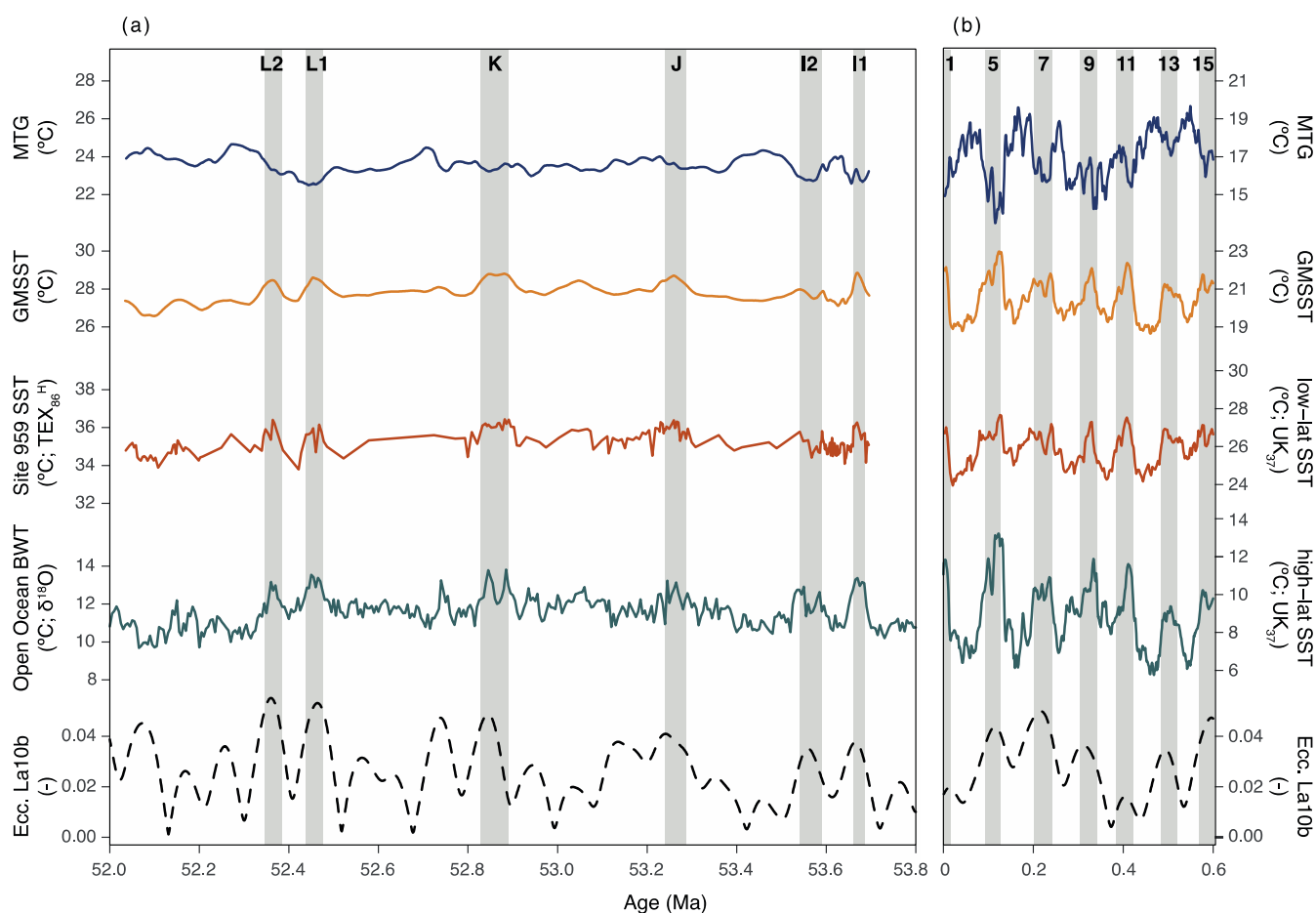


**Figure 5.** Global mean sea surface temperature, meridional temperature gradient and orbital eccentricity for the intervals 53.8–52 Ma (a) and 0.6–0 Ma (b). (a) Early Eocene data with tropical SST data from Site 959 (red) and open ocean BWTs from Westerhold et al. (2020) (green), estimated GMSST (yellow) and MTG (dark blue). (b) Late Pleistocene data with a U<sup>K</sup><sub>37</sub>-based tropical SST compilation by (Herbert et al., 2010) (red) and a U<sup>K</sup><sub>37</sub>-based high-latitude SST dataset averaged from Lawrence et al., (2009); Martínez-García et al. (2010); Ho et al. (2012) (green). Grey bars mark eccentricity related GMSST peaks, i.e. hyperthermals in the early Eocene and interglacials in the late Pleistocene with their respective hyperthermal name or MIS stage number on top. Eccentricity is from the La10b solution (Laskar et al., 2011).



stronger PA than during the early Eocene (Fig. 3b). A general assumption for global climate over glacial-interglacial cycles is that they are largely facilitated by ice-related positive climate feedback mechanisms (Osman et al., 2021). Our data from the ice-free early Eocene, however, imply that eccentricity forcing, through positive climate feedbacks related to the carbon cycle, was capable of producing GMSST variation roughly one third the amplitude of glacial-interglacial variability. It raises the question if similar poorly constrained carbon cycle feedbacks that do not involve ice, snow and frost-related processes were only inherent to past greenhouse climates or if they also played a role in Pleistocene glacial-interglacial climate variability.

## 5. Conclusions

Our new high-resolution SST dataset from the early Eocene tropics confirms that several deep ocean foraminifer  $\delta^{13}\text{C}$  and  $\delta^{18}\text{O}$  isotope events were associated with tropical warming and therefore represent transient global warming events (hyperthermals). The record also shows that SST variability in the tropics was smaller than at high latitudes on timescales of orbital eccentricity. The resulting estimate of PA is 1.7–2.3, within error of previous proxy data-based estimates over longer timespans. Because a major surface albedo feedback contribution from ice can be largely ruled out in our new short-term dataset, we conclude that early Eocene PA is not impacted by non-ice feedback mechanisms that act on  $10^4$ -year timescales or longer. Earth system model simulations generally capture these climate feedbacks relatively well, but may underestimate the strength of non-ice albedo feedbacks and thereby PA in ice-free climate states. Finally, the data suggests eccentricity-forced GMSST changes of up to  $\sim 1^\circ\text{C}$  — even outside the hyperthermals — in the ice-free early Eocene. Such tropical SST and GMSST variability necessitates very strong carbon cycle feedbacks to orbital forcing during that time that may well have been active throughout geological time.

## Data availability

This study's data will be published on Zenodo (DOI: 10.5281/zenodo.8309643).

## Author contributions

CDF and AS designed the research. CDF, DG, LV, MdG, PdR and TA carried out bulk sediment analyses. CA performed calcareous nannofossil paleontology. CDF, FP, TA and AR analyzed lipid biomarkers. CDF, DG, MdG, PdR and TA performed palynology. CDF and XL carried out model comparisons. CDF carried out the data analysis. CDF and AS wrote the paper with feedback from MH, PKB, FP and JF.



## Acknowledgements

This project used samples and data provided by the International Ocean Discovery Program (IODP) and predecessors. We  
440 thank A. van den Dikkenberg, G. Dammers, N. Welters, A. van Dijk, D. Eefting and M. Krasnoperov for technical and  
analytical assistance and H. Kuhlmann and A. Wülbers for support during sampling at Bremen Core Repository (BCR).  
Furthermore, we thank U. Röhl and T. Westerhold (MARUM, Bremen) for discussions regarding Site 959 stratigraphy. This  
project is funded by European Research Council Consolidator Grant 771497 awarded to AS under the Horizon 2020 program.

## Competing interests

445 One of the co-authors is a member of the editorial board of Climate of the Past.

## References

- Agnini, C., Macrì, P., Backman, J., Brinkhuis, H., Fornaciari, E., Giusberti, L., Luciani, V., Rio, D., Sluijs, A., and Speranza, F.: An early Eocene carbon cycle perturbation at ~52.5 Ma in the Southern Alps: Chronology and biotic response, *Paleoceanography*, 24, PA2209, <https://doi.org/10.1029/2008PA001649>, 2009.
- 450 Agnini, C., Fornaciari, E., Raffi, I., Catanzariti, R., Pälike, H., Backman, J., and Rio, D.: Biozonation and biochronology of Paleogene calcareous nannofossils from low and middle latitudes, *nos*, 47, 131–181, <https://doi.org/10.1127/0078-0421/2014/0042>, 2014.
- Anagnostou, E., John, E. H., Babila, T. L., Sexton, P. F., Ridgwell, A., Lunt, D. J., Pearson, P. N., Chalk, T. B., Pancost, R. D., and Foster, G. L.: Proxy evidence for state-dependence of climate sensitivity in the Eocene greenhouse, *Nat Commun*, 11, 4436, <https://doi.org/10.1038/s41467-020-17887-x>, 2020.
- 455 Annan, J. D., Hargreaves, J. C., and Mauritsen, T.: A new global surface temperature reconstruction for the Last Glacial Maximum, *Clim. Past*, 18, 1883–1896, <https://doi.org/10.5194/cp-18-1883-2022>, 2022.
- Besseling, M. A., Hopmans, E. C., Koenen, M., Van Der Meer, M. T. J., Vreugdenhil, S., Schouten, S., Sinninghe Damsté, J. S., and Villanueva, L.: Depth-related differences in archaeal populations impact the isoprenoid tetraether lipid composition of the Mediterranean Sea water column, *Organic Geochemistry*, 135, 16–31, <https://doi.org/10.1016/j.orggeochem.2019.06.008>, 2019.
- 460 Bijl, P. K., Bendle, J. A. P., Bohaty, S. M., Pross, J., Schouten, S., Tauxe, L., Stickley, C. E., McKay, R. M., Röhl, U., Olney, M., Sluijs, A., Escutia, C., Brinkhuis, H., Expedition 318 Scientists, Klaus, A., Fehr, A., Williams, T., Carr, S. A., Dunbar, R. B., González, J. J., Hayden, T. G., Iwai, M., Jimenez-Espejo, F. J., Katsuki, K., Kong, G. S., Nakai, M., Passchier, S., Pekar, S. F., Riesselman, C., Sakai, T., Shrivastava, P. K., Sugisaki, S., Tuo, S., van de Flierdt, T., Welsh, K., and Yamane, M.: Eocene cooling linked to early flow across the Tasmanian Gateway, *Proc. Natl. Acad. Sci. U.S.A.*, 110, 9645–9650, <https://doi.org/10.1073/pnas.1220872110>, 2013.
- 470 Bijl, P. K., Frieling, J., Cramwinckel, M. J., Boschman, C., Sluijs, A., and Peterse, F.: Maastrichtian–Rupelian paleoclimates in the southwest Pacific – a critical re-evaluation of biomarker paleothermometry and dinoflagellate cyst paleoecology at Ocean Drilling Program Site 1172, *Clim. Past*, 17, 2393–2425, <https://doi.org/10.5194/cp-17-2393-2021>, 2021.



- Blaga, C. I., Reichart, G.-J., Heiri, O., and Sinninghe Damsté, J. S.: Tetraether membrane lipid distributions in water-column particulate matter and sediments: a study of 47 European lakes along a north–south transect, *J Paleolimnol*, 41, 523–540, <https://doi.org/10.1007/s10933-008-9242-2>, 2009.
- 475 Caballero, R.: The dynamic range of poleward energy transport in an atmospheric general circulation model, *Geophys. Res. Lett.*, 32, L02705, <https://doi.org/10.1029/2004GL021581>, 2005.
- Caballero, R. and Huber, M.: State-dependent climate sensitivity in past warm climates and its implications for future climate projections, *Proc. Natl. Acad. Sci. U.S.A.*, 110, 14162–14167, <https://doi.org/10.1073/pnas.1303365110>, 2013.
- 480 Carmichael, M. J., Inglis, G. N., Badger, M. P. S., Naafs, B. D. A., Behrooz, L., Rimmelzwaal, S., Monteiro, F. M., Rohrsen, M., Farnsworth, A., Buss, H. L., Dickson, A. J., Valdes, P. J., Lunt, D. J., and Pancost, R. D.: Hydrological and associated biogeochemical consequences of rapid global warming during the Paleocene–Eocene Thermal Maximum, *Global and Planetary Change*, 157, 114–138, <https://doi.org/10.1016/j.gloplacha.2017.07.014>, 2017.
- Cramer, B. S., Wright, J. D., Kent, D. V., and Aubry, M.-P.: Orbital climate forcing of  $\delta^{13}\text{C}$  excursions in the late Paleocene–early Eocene (chrons C24n–C25n), *Paleoceanography*, 18, 1097, <https://doi.org/10.1029/2003PA000909>, 2003.
- 485 Cramwinckel, M. J., Huber, M., Kocken, I. J., Agnini, C., Bijl, P. K., Bohaty, S. M., Frieling, J., Goldner, A., Hilgen, F. J., Kip, E. L., Peterse, F., van der Ploeg, R., Röhl, U., Schouten, S., and Sluijs, A.: Synchronous tropical and polar temperature evolution in the Eocene, *Nature*, 559, 382–386, <https://doi.org/10.1038/s41586-018-0272-2>, 2018.
- Deconto, R. M., Brady, E. C., Bergengren, J., and Hay, W. W.: Late Cretaceous climate, vegetation, and ocean interactions, in: *Warm Climates in Earth History*, edited by: Huber, B. T., Macleod, K. G., and Wing, S. L., Cambridge University Press, 275–296, <https://doi.org/10.1017/CBO9780511564512.010>, 1999.
- 490 Dickens, G. R.: Carbon addition and removal during the Late Palaeocene Thermal Maximum: basic theory with a preliminary treatment of the isotope record at ODP Site 1051, Blake Nose, Geological Society, London, Special Publications, 183, 293–305, <https://doi.org/10.1144/GSL.SP.2001.183.01.14>, 2001.
- Dickens, G. R., Castillo, M. M., and Walker, J. C. G.: A blast of gas in the latest Paleocene: Simulating first-order effects of massive dissociation of oceanic methane hydrate, *Geol*, 25, 259, [https://doi.org/10.1130/0091-7613\(1997\)025<0259:ABOGIT>2.3.CO;2](https://doi.org/10.1130/0091-7613(1997)025<0259:ABOGIT>2.3.CO;2), 1997.
- 495 Dunkley Jones, T., Lunt, D. J., Schmidt, D. N., Ridgwell, A., Sluijs, A., Valdes, P. J., and Maslin, M.: Climate model and proxy data constraints on ocean warming across the Paleocene–Eocene Thermal Maximum, *Earth-Science Reviews*, 125, 123–145, <https://doi.org/10.1016/j.earscirev.2013.07.004>, 2013.
- 500 England, M. R., Eisenman, I., Lutsko, N. J., and Wagner, T. J. W.: The Recent Emergence of Arctic Amplification, *Geophys Res Lett*, 48, <https://doi.org/10.1029/2021GL094086>, 2021.
- Evans, D., Sagoo, N., Renema, W., Cotton, L. J., Müller, W., Todd, J. A., Saraswati, P. K., Stassen, P., Ziegler, M., Pearson, P. N., Valdes, P. J., and Affek, H. P.: Eocene greenhouse climate revealed by coupled clumped isotope-Mg/Ca thermometry, *Proc. Natl. Acad. Sci. U.S.A.*, 115, 1174–1179, <https://doi.org/10.1073/pnas.1714744115>, 2018.
- 505 Frieling, J. and Sluijs, A.: Towards quantitative environmental reconstructions from ancient non-analogue microfossil assemblages: Ecological preferences of Paleocene – Eocene dinoflagellates, *Earth-Science Reviews*, 185, 956–973, <https://doi.org/10.1016/j.earscirev.2018.08.014>, 2018.



- Frieling, J., Gebhardt, H., Huber, M., Adekeye, O. A., Akande, S. O., Reichart, G.-J., Middelburg, J. J., Schouten, S., and Sluijs, A.: Extreme warmth and heat-stressed plankton in the tropics during the Paleocene-Eocene Thermal Maximum, *Sci. Adv.*, 3, e1600891, <https://doi.org/10.1126/sciadv.1600891>, 2017.
- 510 Frieling, J., Peterse, F., Lunt, D. J., Bohaty, S. M., Sinninghe Damsté, J. S., Reichart, G.-J., and Sluijs, A.: Widespread Warming Before and Elevated Barium Burial During the Paleocene-Eocene Thermal Maximum: Evidence for Methane Hydrate Release?, *Paleoceanography and Paleoclimatology*, 34, 546–566, <https://doi.org/10.1029/2018PA003425>, 2019.
- 515 Gaskell, D. E., Huber, M., O'Brien, C. L., Inglis, G. N., Acosta, R. P., Poulsen, C. J., and Hull, P. M.: The latitudinal temperature gradient and its climate dependence as inferred from foraminiferal  $\delta^{18}\text{O}$  over the past 95 million years, *Proc. Natl. Acad. Sci. U.S.A.*, 119, e2111332119, <https://doi.org/10.1073/pnas.2111332119>, 2022.
- Gibbs, S. J., Bown, P. R., Murphy, B. H., Sluijs, A., Edgar, K. M., Pälike, H., Bolton, C. T., and Zachos, J. C.: Scaled biotic disruption during early Eocene global warming events, *Biogeosciences*, 9, 4679–4688, <https://doi.org/10.5194/bg-9-4679-2012>, 2012.
- 520 Harper, D. T., Zeebe, R., Hönisch, B., Schrader, C. D., Lourens, L. J., and Zachos, J. C.: Subtropical sea-surface warming and increased salinity during Eocene Thermal Maximum 2, *Geology*, 46, 187–190, <https://doi.org/10.1130/G39658.1>, 2018.
- Held, I. M. and Soden, B. J.: Robust Responses of the Hydrological Cycle to Global Warming, *Journal of Climate*, 19, 5686–5699, <https://doi.org/10.1175/JCLI3990.1>, 2006.
- 525 Herbert, T. D., Peterson, L. C., Lawrence, K. T., and Liu, Z.: Tropical Ocean Temperatures Over the Past 3.5 Million Years, *Science*, 328, 1530–1534, <https://doi.org/10.1126/science.1185435>, 2010.
- van Hinsbergen, D. J. J., de Groot, L. V., van Schaik, S. J., Spakman, W., Bijl, P. K., Sluijs, A., Langereis, C. G., and Brinkhuis, H.: A Paleolatitude Calculator for Paleoclimate Studies, *PLoS ONE*, 10, e0126946, <https://doi.org/10.1371/journal.pone.0126946>, 2015.
- 530 Ho, S. L. and Laepple, T.: Flat meridional temperature gradient in the early Eocene in the subsurface rather than surface ocean, *Nature Geosci*, 9, 606–610, <https://doi.org/10.1038/ngeo2763>, 2016.
- Ho, S. L., Mollenhauer, G., Lamy, F., Martínez-García, A., Mohtadi, M., Gersonde, R., Hebbeln, D., Nunez-Ricardo, S., Rosell-Melé, A., and Tiedemann, R.: Sea surface temperature variability in the Pacific sector of the Southern Ocean over the past 700 kyr, *Paleoceanography*, 27, <https://doi.org/10.1029/2012PA002317>, 2012.
- 535 Hollis, C. J., Taylor, K. W. R., Handley, L., Pancost, R. D., Huber, M., Creech, J. B., Hines, B. R., Crouch, E. M., Morgans, H. E. G., Crampton, J. S., Gibbs, S., Pearson, P. N., and Zachos, J. C.: Early Paleogene temperature history of the Southwest Pacific Ocean: Reconciling proxies and models, *Earth and Planetary Science Letters*, 349–350, 53–66, <https://doi.org/10.1016/j.epsl.2012.06.024>, 2012.
- 540 Hopmans, E. C., Weijers, J. W. H., Schefuß, E., Herfort, L., Sinninghe Damsté, J. S., and Schouten, S.: A novel proxy for terrestrial organic matter in sediments based on branched and isoprenoid tetraether lipids, *Earth and Planetary Science Letters*, 224, 107–116, <https://doi.org/10.1016/j.epsl.2004.05.012>, 2004.
- Hopmans, E. C., Schouten, S., and Sinninghe Damsté, J. S.: The effect of improved chromatography on GDGT-based palaeoproxies, *Organic Geochemistry*, 93, 1–6, <https://doi.org/10.1016/j.orggeochem.2015.12.006>, 2016.



- 545 Hurley, S. J., Lipp, J. S., Close, H. G., Hinrichs, K.-U., and Pearson, A.: Distribution and export of isoprenoid tetraether lipids in suspended particulate matter from the water column of the Western Atlantic Ocean, *Organic Geochemistry*, 116, 90–102, <https://doi.org/10.1016/j.orggeochem.2017.11.010>, 2018.
- 550 Inglis, G. N., Bragg, F., Burls, N. J., Cramwinckel, M. J., Evans, D., Foster, G. L., Huber, M., Lunt, D. J., Siler, N., Steinig, S., Tierney, J. E., Wilkinson, R., Anagnostou, E., de Boer, A. M., Dunkley Jones, T., Edgar, K. M., Hollis, C. J., Hutchinson, D. K., and Pancost, R. D.: Global mean surface temperature and climate sensitivity of the early Eocene Climatic Optimum (EECO), Paleocene–Eocene Thermal Maximum (PETM), and latest Paleocene, *Clim. Past*, 16, 1953–1968, <https://doi.org/10.5194/cp-16-1953-2020>, 2020.
- Karner, M. B., DeLong, E. F., and Karl, D. M.: Archaeal dominance in the mesopelagic zone of the Pacific Ocean, 409, 4, 2001.
- 555 Kennett, J. P. and Stott, L. D.: Abrupt deep-sea warming, palaeoceanographic changes and benthic extinctions at the end of the Palaeocene, *Nature*, 353, 225–229, <https://doi.org/10.1038/353225a0>, 1991.
- Kim, J.-H., van der Meer, J., Schouten, S., Helmke, P., Willmott, V., Sangiorgi, F., Koç, N., Hopmans, E. C., and Damsté, J. S. S.: New indices and calibrations derived from the distribution of crenarchaeal isoprenoid tetraether lipids: Implications for past sea surface temperature reconstructions, *Geochimica et Cosmochimica Acta*, 74, 4639–4654, <https://doi.org/10.1016/j.gca.2010.05.027>, 2010.
- 560 Lauretano, V., Zachos, J. C., and Lourens, L. J.: Orbitally Paced Carbon and Deep-Sea Temperature Changes at the Peak of the Early Eocene Climatic Optimum, *Paleoceanography and Paleoclimatology*, 33, 1050–1065, <https://doi.org/10.1029/2018PA003422>, 2018.
- 565 Lawrence, K. T., Herbert, T. D., Brown, C. M., Raymo, M. E., and Haywood, A. M.: High-amplitude variations in North Atlantic sea surface temperature during the early Pliocene warm period, *Paleoceanography*, 24, PA2218, <https://doi.org/10.1029/2008PA001669>, 2009.
- Leon-Rodriguez, L. and Dickens, G. R.: Constraints on ocean acidification associated with rapid and massive carbon injections: The early Paleogene record at ocean drilling program site 1215, equatorial Pacific Ocean, *Palaeogeography, Palaeoclimatology, Palaeoecology*, 298, 409–420, <https://doi.org/10.1016/j.palaeo.2010.10.029>, 2010.
- 570 Liu, X., Huber, M., Foster, G. L., Dessler, A., and Zhang, Y. G.: Persistent high latitude amplification of the Pacific Ocean over the past 10 million years, *Nat Commun*, 13, 7310, <https://doi.org/10.1038/s41467-022-35011-z>, 2022.
- Lourens, L. J., Sluijs, A., Kroon, D., Zachos, J. C., Thomas, E., Röhl, U., Bowles, J., and Raffi, I.: Astronomical pacing of late Palaeocene to early Eocene global warming events, *Nature*, 435, 1083–1087, <https://doi.org/10.1038/nature03814>, 2005.
- 575 Lunt, D. J., Bragg, F., Chan, W.-L., Hutchinson, D. K., Ladant, J.-B., Morozova, P., Niezgodzki, I., Steinig, S., Zhang, Z., Zhu, J., Abe-Ouchi, A., Anagnostou, E., de Boer, A. M., Coxall, H. K., Donnadiou, Y., Foster, G., Inglis, G. N., Knorr, G., Langebroek, P. M., Lear, C. H., Lohmann, G., Poulsen, C. J., Sepulchre, P., Tierney, J. E., Valdes, P. J., Volodin, E. M., Jones, T. D., Hollis, C. J., Huber, M., and Otto-Bliesner, L.: DeepMIP: Model intercomparison of early Eocene climatic optimum (EECO) large-scale climate features and comparison with proxy data, *Clim. Past*, 17, 203–227, 2021.
- 580



- Martínez-García, A., Rosell-Melé, A., McClymont, E. L., Gersonde, R., and Haug, G. H.: Subpolar Link to the Emergence of the Modern Equatorial Pacific Cold Tongue, *Science*, 328, 1550–1553, <https://doi.org/10.1126/science.1184480>, 2010.
- 585 Mascle, J., Lohmann, G. P., Clift, P. D., and Shipboard Scientific Party (Eds.): Proceedings of the Ocean Drilling Program, 159 Initial Reports, Ocean Drilling Program, <https://doi.org/10.2973/odp.proc.ir.159.1996>, 1996.
- Massana, R., DeLong, E. F., and Pedrós-Alió, C.: A Few Cosmopolitan Phylotypes Dominate Planktonic Archaeal Assemblages in Widely Different Oceanic Provinces, *Appl Environ Microbiol*, 66, 1777–1787, <https://doi.org/10.1128/AEM.66.5.1777-1787.2000>, 2000.
- 590 Masson-Delmotte, V., Schulz, M., Abe-Ouchi, A., Beer, J., Ganopolski, A., Gonzalez Rouco, J. F., Jansen, E., Lambeck, K., Luterbacher, J., Naish, T., Osborn, T., Otto-Bliesner, B., Quinn, T., Ramesh, R., Rojas, M., Shao, X., and Timmermann, A.: Information from paleoclimate archives, in: *Climate change 2013: the physical science basis*, edited by: Stocker, T. F., Qin, D., Plattner, G.-K., Tignor, M. M. B., Allen, S. K., Boschung, J., Nauels, A., Xia, Y., Bex, V., and Midgley, P. M., Cambridge University Press, 383–464, <https://doi.org/10.1017/CBO9781107415324.013>, 2013.
- 595 McInerney, F. A. and Wing, S. L.: The Paleocene-Eocene Thermal Maximum: A Perturbation of Carbon Cycle, Climate, and Biosphere with Implications for the Future, *Annu. Rev. Earth Planet. Sci.*, 39, 489–516, <https://doi.org/10.1146/annurev-earth-040610-133431>, 2011.
- 600 O’Brien, C. L., Robinson, S. A., Pancost, R. D., Sinninghe Damsté, J. S., Schouten, S., Lunt, D. J., Alsenz, H., Bornemann, A., Bottini, C., Brassell, S. C., Farnsworth, A., Forster, A., Huber, B. T., Inglis, G. N., Jenkyns, H. C., Linnert, C., Littler, K., Markwick, P., McAnena, A., Mutterlose, J., Naafs, B. D. A., Püttmann, W., Sluijs, A., van Helmond, N. A. G. M., Vellekoop, J., Wagner, T., and Wrobel, N. E.: Cretaceous sea-surface temperature evolution: Constraints from TEX86 and planktonic foraminiferal oxygen isotopes, *Earth-Science Reviews*, 172, 224–247, <https://doi.org/10.1016/j.earscirev.2017.07.012>, 2017.
- 605 Osman, M. B., Tierney, J. E., Zhu, J., Tardif, R., Hakim, G. J., King, J., and Poulsen, C. J.: Globally resolved surface temperatures since the Last Glacial Maximum, *Nature*, 599, 239–244, <https://doi.org/10.1038/s41586-021-03984-4>, 2021.
- PALAEOSSENS Project Members: Making sense of palaeoclimate sensitivity, *Nature*, 491, 683–691, <https://doi.org/10.1038/nature11574>, 2012.
- 610 van der Ploeg, R., Selby, D., Cramwinckel, M. J., Li, Y., Bohaty, S. M., Middelburg, J. J., and Sluijs, A.: Middle Eocene greenhouse warming facilitated by diminished weathering feedback, *Nat Commun*, 9, 2877, <https://doi.org/10.1038/s41467-018-05104-9>, 2018.
- 615 Pross, J., Contreras, L., Bijl, P. K., Greenwood, D. R., Bohaty, S. M., Schouten, S., Bendle, J. A., Röhl, U., Tauxe, L., Raine, J. I., Huck, C. E., van de Flierdt, T., Jamieson, S. S. R., Stickley, C. E., van de Schootbrugge, B., Escutia, C., Brinkhuis, H., and Integrated Ocean Drilling Program Expedition 318 Scientists: Persistent near-tropical warmth on the Antarctic continent during the early Eocene epoch, *Nature*, 488, 73–77, <https://doi.org/10.1038/nature11300>, 2012.
- Rattanasriampaipong, R., Zhang, Y. G., Pearson, A., Hedlund, B. P., and Zhang, S.: Archaeal lipids trace ecology and evolution of marine ammonia-oxidizing archaea, *Proc. Natl. Acad. Sci. U.S.A.*, 119, e2123193119, <https://doi.org/10.1073/pnas.2123193119>, 2022.



- 620 Schouten, S., Hopmans, E. C., Schefuß, E., and Sinninghe Damsté, J. S.: Distributional variations in marine crenarchaeotal membrane lipids: a new tool for reconstructing ancient sea water temperatures?, *Earth and Planetary Science Letters*, 204, 265–274, [https://doi.org/10.1016/S0012-821X\(02\)00979-2](https://doi.org/10.1016/S0012-821X(02)00979-2), 2002.
- Sinninghe Damsté, J. S., Rijpstra, W. I. C., Hopmans, E. C., Prahl, F. G., Wakeham, S. G., and Schouten, S.: Distribution of Membrane Lipids of Planktonic *Crenarchaeota* in the Arabian Sea, *Appl Environ Microbiol*, 68, 2997–3002, <https://doi.org/10.1128/AEM.68.6.2997-3002.2002>, 2002.
- 625
- Slotnick, B. S., Dickens, G. R., Nicolo, M. J., Hollis, C. J., Crampton, J. S., Zachos, J. C., and Sluijs, A.: Large-Amplitude Variations in Carbon Cycling and Terrestrial Weathering during the Latest Paleocene and Earliest Eocene: The Record at Mead Stream, New Zealand, *The Journal of Geology*, 120, 487–505, <https://doi.org/10.1086/666743>, 2012.
- Sluijs, A., Pross, J., and Brinkhuis, H.: From greenhouse to icehouse; organic-walled dinoflagellate cysts as paleoenvironmental indicators in the Paleogene, *Earth-Science Reviews*, 68, 281–315, <https://doi.org/10.1016/j.earscirev.2004.06.001>, 2005.
- 630
- Sluijs, A., Schouten, S., Donders, T. H., Schoon, P. L., Röhl, U., Reichert, G.-J., Sangiorgi, F., Kim, J.-H., Sinninghe Damsté, J. S., and Brinkhuis, H.: Warm and wet conditions in the Arctic region during Eocene Thermal Maximum 2, *Nature Geosci*, 2, 777–780, <https://doi.org/10.1038/ngeo668>, 2009.
- Sluijs, A., Frieling, J., Inglis, G. N., Nierop, K. G. J., Peterse, F., Sangiorgi, F., and Schouten, S.: Late Paleocene–early Eocene Arctic Ocean sea surface temperatures: reassessing biomarker paleothermometry at Lomonosov Ridge, *Clim. Past*, 16, 2381–2400, <https://doi.org/10.5194/cp-16-2381-2020>, 2020.
- 635
- Stap, L., Sluijs, A., Thomas, E., and Lourens, L.: Patterns and magnitude of deep sea carbonate dissolution during Eocene Thermal Maximum 2 and H2, *Walvis Ridge, southeastern Atlantic Ocean, Paleocyanography*, 24, PA1211, <https://doi.org/10.1029/2008PA001655>, 2009.
- 640
- Stap, L., Lourens, L. J., Thomas, E., Sluijs, A., Bohaty, S., and Zachos, J. C.: High-resolution deep-sea carbon and oxygen isotope records of Eocene Thermal Maximum 2 and H2, *Geology*, 38, 607–610, <https://doi.org/10.1130/G30777.1>, 2010.
- Stockmarr, J.: Tablets with spores used in absolute pollen analysis, *Pollen Spores*, 13, 615–621, 1972.
- 645
- Stuecker, M. F., Bitz, C. M., Armour, K. C., Proistosescu, C., Kang, S. M., Xie, S.-P., Kim, D., McGregor, S., Zhang, W., Zhao, S., Cai, W., Dong, Y., and Jin, F.-F.: Polar amplification dominated by local forcing and feedbacks, *Nature Clim Change*, 8, 1076–1081, <https://doi.org/10.1038/s41558-018-0339-y>, 2018.
- Taylor, K. W. R., Huber, M., Hollis, C. J., Hernandez-Sanchez, M. T., and Pancost, R. D.: Re-evaluating modern and Palaeogene GDGT distributions: Implications for SST reconstructions, *Global and Planetary Change*, 108, 158–174, <https://doi.org/10.1016/j.gloplacha.2013.06.011>, 2013a.
- 650
- Taylor, P. C., Cai, M., Hu, A., Meehl, J., Washington, W., and Zhang, G. J.: A Decomposition of Feedback Contributions to Polar Warming Amplification, *Journal of Climate*, 26, 7023–7043, <https://doi.org/10.1175/JCLI-D-12-00696.1>, 2013b.
- 655
- Thomas, E. and Zachos, J. C.: Was the late Paleocene thermal maximum a unique event?, *GFF*, 122, 169–170, <https://doi.org/10.1080/11035890001221169>, 2000.





- Tierney, J. E., Zhu, J., Li, M., Ridgwell, A., Hakim, G. J., Poulsen, C. J., Whiteford, R. D. M., Rae, J. W. B., and Kump, L. R.: Spatial patterns of climate change across the Paleocene–Eocene Thermal Maximum, *Proceedings of the National Academy of Sciences*, 119, e2205326119, <https://doi.org/10.1073/pnas.2205326119>, 2022.
- 660 Vervoort, P., Kirtland Turner, S., Rochholz, F., and Ridgwell, A.: Earth System Model Analysis of How Astronomical Forcing Is Imprinted Onto the Marine Geological Record: The Role of the Inorganic (Carbonate) Carbon Cycle and Feedbacks, *Paleoceanogr Paleoclimatol*, 36, <https://doi.org/10.1029/2020PA004090>, 2021.
- Wagner, T.: Late Cretaceous to early Quaternary organic sedimentation in the eastern Equatorial Atlantic, *Palaeogeography, Palaeoclimatology, Palaeoecology*, 179, 113–147, [https://doi.org/10.1016/S0031-0182\(01\)00415-1](https://doi.org/10.1016/S0031-0182(01)00415-1), 2002.
- 665 Weijers, J. W. H., Lim, K. L. H., Aquilina, A., Sinninghe Damsté, J. S., and Pancost, R. D.: Biogeochemical controls on glycerol dialkyl glycerol tetraether lipid distributions in sediments characterized by diffusive methane flux, *Geochem. Geophys. Geosyst.*, 12, Q10010, <https://doi.org/10.1029/2011GC003724>, 2011.
- van der Weijst, C. M. H., van der Laan, K. J., Peterse, F., Reichert, G.-J., Sangiorgi, F., Schouten, S., Veenstra, T. J. T., and Sluijs, A.: A 15-million-year surface- and subsurface-integrated TEX<sub>86</sub> temperature record from the eastern equatorial Atlantic, *Climate of the Past*, 18, 1947–1962, <https://doi.org/10.5194/cp-18-1947-2022>, 2022.
- 670 Westerhold, T., Röhl, U., Frederichs, T., Agnini, C., Raffi, I., Zachos, J. C., and Wilkens, R. H.: Astronomical calibration of the Ypresian timescale: implications for seafloor spreading rates and the chaotic behavior of the solar system?, *Clim. Past*, 13, 1129–1152, <https://doi.org/10.5194/cp-13-1129-2017>, 2017.
- Westerhold, T., Röhl, U., Donner, B., and Zachos, J. C.: Global Extent of Early Eocene Hyperthermal Events: A New Pacific Benthic Foraminiferal Isotope Record From Shatsky Rise (ODP Site 1209), *Paleoceanography and Paleoclimatology*, 33, 626–642, <https://doi.org/10.1029/2017PA003306>, 2018.
- 675 Westerhold, T., Marwan, N., Drury, A. J., Liebrand, D., Agnini, C., Anagnostou, E., Barnet, J. S. K., Bohaty, S. M., De Vleeschouwer, D., Florindo, F., Frederichs, T., Hodell, D. A., Holbourn, A. E., Kroon, D., Laurentano, V., Littler, K., Lourens, L. J., Lyle, M., Pälike, H., Röhl, U., Tian, J., Wilkens, R. H., Wilson, P. A., and Zachos, J. C.: An astronomically dated record of Earth’s climate and its predictability over the last 66 million years, *Science*, 369, 1383–1387, <https://doi.org/10.1126/science.aba6853>, 2020.
- 680 Willard, D. A., Donders, T. H., Reichgelt, T., Greenwood, D. R., Sangiorgi, F., Peterse, F., Nierop, K. G. J., Frieling, J., Schouten, S., and Sluijs, A.: Arctic vegetation, temperature, and hydrology during Early Eocene transient global warming events, *Global and Planetary Change*, 178, 139–152, <https://doi.org/10.1016/j.gloplacha.2019.04.012>, 2019.
- Wuchter, C., Schouten, S., Wakeham, S. G., and Sinninghe Damsté, J. S.: Archaeal tetraether membrane lipid fluxes in the northeastern Pacific and the Arabian Sea: Implications for TEX<sub>86</sub> paleothermometry, *Paleoceanography*, 21, <https://doi.org/10.1029/2006PA001279>, 2006.
- 685 Zachos, J., Pagani, M., Sloan, L., Thomas, E., and Billups, K.: Trends, Rhythms, and Aberrations in Global Climate 65 Ma to Present, *Science*, 292, 686–693, <https://doi.org/10.1126/science.1059412>, 2001.
- 690 Zachos, J. C., Röhl, U., Schellenberg, S. A., Sluijs, A., Hodell, D. A., Kelly, D. C., Thomas, E., Nicolo, M., Raffi, I., Lourens, L. J., McCarren, H., and Kroon, D.: Rapid Acidification of the Ocean During the Paleocene-Eocene Thermal Maximum, *Science*, 308, 1611–1615, <https://doi.org/10.1126/science.1109004>, 2005.



- Zachos, J. C., McCarren, H., Murphy, B., Röhl, U., and Westerhold, T.: Tempo and scale of late Paleocene and early Eocene carbon isotope cycles: Implications for the origin of hyperthermals, *Earth and Planetary Science Letters*, 299, 242–249, <https://doi.org/10.1016/j.epsl.2010.09.004>, 2010.
- 695 Zeebe, R. E., Westerhold, T., Littler, K., and Zachos, J. C.: Orbital forcing of the Paleocene and Eocene carbon cycle, *Paleoceanography*, 32, 440–465, <https://doi.org/10.1002/2016PA003054>, 2017.
- Zhang, Y., Huck, T., Lique, C., Donnadieu, Y., Ladant, J.-B., Rabineau, M., and Aslanian, D.: Early Eocene vigorous ocean overturning and its contribution to a warm Southern Ocean, *Clim. Past*, 16, 1263–1283, <https://doi.org/10.5194/cp-16-1263-2020>, 2020.
- 700 Zhang, Y. G., Zhang, C. L., Liu, X.-L., Li, L., Hinrichs, K.-U., and Noakes, J. E.: Methane Index: A tetraether archaeal lipid biomarker indicator for detecting the instability of marine gas hydrates, *Earth and Planetary Science Letters*, 307, 525–534, <https://doi.org/10.1016/j.epsl.2011.05.031>, 2011.
- Zhang, Y. G., Pagani, M., and Wang, Z.: Ring Index: A new strategy to evaluate the integrity of TEX<sub>86</sub> paleothermometry, *Paleoceanography*, 31, 220–232, <https://doi.org/10.1002/2015PA002848>, 2016.

705